JGR Space Physics

RESEARCH ARTICLE
10.1029/2024JA032528

Statistics and Models of the Electron Plasma Density From the Van Allen Probes

J.-F. Ripoll[1,2], S. A. Thaller[3,4], D. P. Hartley[5], D. M. Malaspina[3,6], W. S. Kurth[5], G. S. Cunningham[7], V. Pierrard[8,9], and J. Wygant[10]

[1]CEA, DAM, DIF, Arpajon, France, [2]UPS, CEA, LMCE, Bruyères-le-Châtel, France, [3]Laboratory for Atmospheric and Space Physics, University of Colorado, Boulder, Boulder, CO, USA, [4]Now at Orion Space Solutions, An Arcfield Company, Louisville, CO, USA, [5]Department of Physics and Astronomy, University of Iowa, Iowa City, IA, USA, [6]Astrophysical and Planetary Sciences Department, University of Colorado, Boulder, Boulder, CO, USA, [7]Space Science and Applications Group, Los Alamos National Laboratory, Los Alamos, NM, USA, [8]Department Space Physics and Solar-Terrestrial Center of Excellence, Royal Belgian Institute for Space Aeronomy, Brussels, Belgium, [9]Center for Space Radiations, Earth and Life Institute - Climate Sciences (ELIC), Université Catholique de Louvain, Louvain-La-Neuve, Belgium, [10]School of Physics and Astronomy, University of Minnesota, Minneapolis, MN, USA

Key Points:

- Generation of new statistics of mean and standard deviation of the plasma density from Electric Field and Waves and Electric and Magnetic Field Instrument Suite and Integrated Science of RBSP for the whole mission
- Empirical density models made of fits are provided versus L-shell, magnetic local time (MLT), and geomagnetic indices to be used in radiation belt codes
- An extensive analysis of the cold plasma statistics is provided with respect to L-shell, MLT, and geomagnetic activity

Correspondence to:
J.-F. Ripoll,
jean-francois.ripoll@cea.fr

Citation:
Ripoll, J.-F., Thaller, S. A., Hartley, D. P., Malaspina, D. M., Kurth, W. S., Cunningham, G. S., et al. (2024). Statistics and models of the electron plasma density from the Van Allen Probes. *Journal of Geophysical Research: Space Physics*, *129*, e2024JA032528. https://doi.org/10.1029/2024JA032528

Received 7 FEB 2024
Accepted 16 JUL 2024

Author Contributions:
Conceptualization: J.-F. Ripoll, S. A. Thaller, D. P. Hartley
Data curation: S. A. Thaller, D. P. Hartley, J. Wygant
Formal analysis: J.-F. Ripoll, S. A. Thaller, D. P. Hartley
Funding acquisition: J.-F. Ripoll, S. A. Thaller, D. P. Hartley, D. M. Malaspina, W. S. Kurth, G. S. Cunningham, V. Pierrard, J. Wygant
Investigation: J.-F. Ripoll, S. A. Thaller, D. P. Hartley
Methodology: J.-F. Ripoll, S. A. Thaller, D. P. Hartley, W. S. Kurth, J. Wygant
Project administration: J.-F. Ripoll
Software: S. A. Thaller, D. P. Hartley
Supervision: J.-F. Ripoll
Validation: J.-F. Ripoll, S. A. Thaller, D. P. Hartley, D. M. Malaspina, W. S. Kurth, G. S. Cunningham, V. Pierrard
Visualization: S. A. Thaller, D. P. Hartley
Writing – original draft: J.-F. Ripoll

Abstract We use the full NASA Van Allen Probes mission (2012–2019) to extract the electron plasma density from the Electric and Magnetic Field Instrument Suite and Integrated Science (EMFISIS) and Electric Field and Waves (EFW) instruments and discuss the evolution of the plasmasphere. We generate new statistics including mean and standard deviations of the plasma density with respect to L-shell, magnetic local time (MLT), and various geomagnetic indices. These statistics are generated to be applied in radiation belt physics and space weather codes (with fits provided). The mean plasmasphere is circular around Earth with respect to MLT for Kp < 1. The mean 100 cm^{-3} level line is above L = 5 and mean 10 cm^{-3} level expands above the Van Allen Probes apogee for Kp < 1. The outer electron belt lies within the plasmasphere for 60% of all times. As activity increases (Kp > 2), a gradual MLT asymmetry forms with higher mean density in the afternoon sector due to plumes expanding outward. Conversely, the mean density decreases on the dawn and night sectors. The mean density is between ~500 and ~50 cm^{-3} between L ~ 4 and L ~ 6 during quiet and moderately active times (Kp < 3), representing ~80% of all times. Statistics in regions of high density below L = 2 are underdefined for intense activity. The highest standard deviation of density represents a factor 2.5 to 3 times the mean above L = 5 and for active times. We find the percent difference between the EFW and EMFISIS densities is bounded by ±20% for quiet and moderate activity (Kp < 5) and goes up to ±100% for extreme activity.

Plain Language Summary The Earth's plasmasphere, discovered in the 1950s, is a region of cold plasma made of ions and electrons of a few electronvolts in energy, originating from upwelling ionized gas from the ionosphere and forming a rotating torus around the Earth. The radial profile of the electron cold plasma density within the plasmasphere decays from 10,000 electrons per cubic centimeter at ~1,000 km altitude to 10s electrons per cubic centimeter at its outer edge, sometimes exceeding ~36,000 km in altitude at the equator. The state of the plasmasphere is highly dependent on geomagnetic conditions, with geomagnetic storms and substorms eroding parts of this plasma. Here, we analyze 7 years of NASA Van Allen Probes measurements of the electron plasma density and generate statistics with respect to L-shell, magnetic local time, and geomagnetic indices. In this way, we show statistical variations of the plasmasphere, a strong magnetic local time dependence, and erosion with increasing geomagnetic activity. New mean electron densities and their standard deviation are generated and fitted with model functions that can be incorporated into space weather codes. This is important because the electron density is a key parameter influencing the strength of wave-particle interactions that accelerate and scatter energetic particles in the inner magnetosphere.

1. Introduction

The Earth's plasmasphere is a region of cold plasma made of H^+, O^+, He^+ and electrons of a few electronvolts, originating from the ionosphere and forming a rotating torus that surrounds the Earth and forms the innermost part of the magnetosphere (e.g., Carpenter, 1963). It was discovered in the 1950–1960's (Carpenter, 1963, 1966; Gringauz et al., 1960, 1962; Storey, 1953) (see historical review in Lemaire and Gringauz, 1998; Kotova, 2007). The radial profile of the electron density within the plasmasphere presents a gradual, statistical, decay from $n_e \sim 10^4$ cm^{-3} at the lowest L-shell (L) to ~10–100 cm^{-3} (depending on the authors) at its outer edge, the

Writing – review & editing: J.-F. Ripoll, S. A. Thaller, D. P. Hartley, D. M. Malaspina, W. S. Kurth, G. S. Cunningham, V. Pierrard

plasmapause (e.g., Lemaire and Gringauz, 1998). Plasmaspheric plasma has been found up to L = 9 at high latitude (33°) on the dawn side (Denton et al., 2004).

The plasmasphere's structure and composition evolve drastically under the influence of its environment and geomagnetic activity. Geomagnetic disturbances move the plasmapause inward to smaller L values (Carpenter, 1970; Chappell et al., 1970). The plasmasphere builds up from ionospheric refilling during geomagnetically quiet intervals and storm recovery periods and shrinks due to erosion during active periods of geomagnetic storms and substorms (e.g., Carpenter and Lemaire, 1997). Strong erosion starts first by sunward convection and expansion of the plasmaspheric plasma on the dayside. This sunward convection is itself caused by dayside magnetopause reconnection (Dungey, 1961) of the Earth's magnetic field with the Interplanetary Magnetic Field (IMF) during geomagnetic disturbances (e.g., Carpenter et al., 1993; Goldstein et al., 2003a, 2005; Spasojevic et al., 2003). The dayside extended plasmaspheric plasma forms what is commonly called a plume: a detached plasma element or a plasmaspheric tail, which then spreads eastward and narrows in magnetic local time (MLT). The plume rotates eastward with the main plasmasphere body and wraps up around it. The separated phases of the erosion motion are described in more detail in Goldstein et al. (2005). Erosion and plume narrowing can be enhanced by the electric field of Sub-Auroral Polarization Stream (SAPS) (e.g., Lejosne and Mozer, 2017 and references therein), which causes the plasmapause to move Earthward on the dusk side and narrows duskside plumes (Goldstein et al., 2003b). As they drift, plumes can cross the outer electron radiation belt (Borovsky et al., 2014) and change significantly the intensity of wave particle interactions in that region (e.g., Dahmen et al., 2022; Millan et al., 2021). At geosynchronous orbit, plumes generally persist for 4 days and drain about half of the outer plasmasphere within the first 20 hr following a storm, with a rate of 1.2 tons/hr of protons leading to 34 tons of protons being transported by plumes during the life of a storm (Borovsky and Denton, 2008). As recovery starts and the magnetosphere experiences weaker disturbances from the solar wind, the plasmasphere starts refilling. The refilling process remains an open problem, with needed future observations and science developments identified in Goldstein et al. (2023). For instance, Reinisch et al. (2004) have shown that when the plasmasphere was depleted during the 31 March 2001 magnetic storm, refilling took less than 28 hr to reach the average level, significantly faster than the theoretical prediction of 2–3 days from Tu et al. (2003) model. Ionospheric refilling becomes the dominant process during prolonged periods of very quiet geomagnetic conditions. Long-term (>1 day) density refilling rates extracted from IMAGE/RPI data during quiet times (Kp < 1.5) are reported in Denton et al. (2012).

The plasmasphere density is difficult to detect at both of its dense ($>10^3$ cm^{-3}) and diluted (<100 cm^{-3}) limits (reasons why are discussed in Section 2.1). These large/low values also occur commonly within the main plasmasphere body, originating from various internal structures of various spatial scales that contribute to make the plasmasphere a dynamically complex, and sometimes turbulent (e.g., LeDocq et al., 1994) structure which remains difficult to measure in a systematic and continuous way. Fine scale density structures are observed and discussed, for instance, in Chappell (1974), LeDocq et al. (1994), and Darrouzet et al. (2004). Density inhomogeneities have also recently been detected in the boundary layer of the plasmasphere (Kotova et al., 2023). Carpenter and Lemaire (1997) suggested that numerous processes associated to the time-varying, structured, night-side electric field could support the development of these multi-scale structures. These include; (a) turbulence created in dense plasma under enhanced flow speed; (b) shear flow instability in regions of subauroral ion drifts (SAID) (Anderson et al., 2001); (c) gradient drift instability in the region of steep plasmapause density gradients; and (d) gravitational interchange instability in regions where fast eastward drifts occur. The fine scale structure of the outer plasmasphere was reported by Moldwin et al. (1995) with structures of the order of 1,000 km or less. In the dusk sector of the outer plasmasphere, these authors suggest the structures are caused by penetrating substorm electric fields.

Plume merging is another theoretical way of generating fine plasmaspheric structure from successive layers of wrapped residual plumes which merge with newer plumes, creating layers of filamentary density structure over multiple cycles (e.g., Goldstein et al., 2003b; Sandel et al., 2003). The development and motion of plumes is particularly well understood from IMAGE measurements as well as E × B-driven plasmapause test particle (PTP) codes (Goldstein, 2006; Nishida, 1966). This model has been found to reproduce the density dynamics of the rotating plumes adequately enough to interpret Van Allen Probes observations (e.g., Goldstein et al., 2014a, 2014b). Models of the plasma density in the framework of radiation belt physics and space weather codes, including ionospheric source models, empirical density models, physics-based and machine-learning density models, are reviewed in Ripoll et al. (2023). The empirical models of Carpenter and Anderson (1992), Gallagher

et al. (2000), Denton et al. (2006), Sheeley et al. (2001) and Ozhogin et al. (2012) are compared in Figure 8 of Ozhogin et al. (2012). INTERBALL-1 spacecraft density statistics have recently been published in Kotova and Bezrukikh (2022) covering the Earth equatorial plane from L = 1.4 to L = 6 radii (see their Figure 7 with a comparison with known models). Variations in the electron plasma density inferred from the upper hybrid resonance on Arase (Miyoshi et al., 2018), and hiss-inferred density values (Hartley et al., 2018a, 2018b) from Van Allen Probes (Mauk et al., 2013) were investigated at low L-shells (L < 3) in Hartley et al. (2023). A clear MLT dependence of the plasma density was identified, which was not found or included in some previous models. Hartley et al. (2023) derived a new empirical density model, taking the model of Ozhogin et al. (2012) as the basis of its functional form, extending the model range inwards from L = 1.6 to L = 1.1 and adding an MLT dependence.

Darrouzet and De Keyser (2013) review the studies of the Earth's plasmasphere following the ESA Cluster and NASA IMAGE missions. The latter provided, for the first time, global EUV images of the plasmasphere showing its variability (Darrouzet, De Keyser, Pierrard, 2009; Darrouzet et al., 2009). Certain features and behaviors of the plasmasphere appear frequently in the EUV images such as shoulders on the plasmapause equatorial projection (Pierrard and Cabrera, 2005), channels (i.e., narrow regions of decreased plasma content extended along latitude), notches (i.e., narrow voids restricted in latitude), and various plume forms (Sandel et al., 2003). Goldstein (2006) provides a review of the plasmasphere response to geomagnetic activity written as a tutorial in a way that is accessible to all. Kotova (2007) reviewed the state of plasmasphere studies, including Russian observations and studies. A review of the known impact of the cold-ion and cold-electron populations in the Earth's magnetosphere is available in Delzanno et al. (2021) with focus on the source of hot magnetospheric plasma, solar-wind/magnetosphere coupling, magnetotail reconnection and substorms, Kelvin–Helmholtz instabilities on the magnetopause, wave–particle interactions, aurora structuring and spacecraft charging.

Electron plasma density values inferred from measurements by the NASA Van Allen Probes mission (2012–2019) (Mauk et al., 2013) are used here as well as in Ripoll et al. (2022), in order to extract empirical plasmapause models (such as $L_{100/pp} = b - aKp^*$) versus L, MLT and various geomagnetic indices, similarly to what is done in this article for the plasmaspheric density. These models are thus fully compatible with this study. The plasmapause is computed with two methods. The first method computes a density gradient, L_{pp}, when it exists, a hard plasmapause (e.g., Carpenter, 1966; Carpenter and Anderson, 1992; Moldwin et al., 2002; O'Brien and Moldwin, 2003). The second considers a dense outer edge of the plasmasphere close to the 100 cm^{-3} density level, L_{100}, a soft plasmapause (Carpenter, 1966). Both are extensively discussed and compared with the Carpenter and Anderson 1992 model. Ripoll et al. (2022) show the two methods, L_{pp} versus L_{100}, converge toward each other, with differences within less than [−0.5 L, 0.5 L] for 86% of cases (considering ∼14,907 plasmapause positions from 2012 to 2019). The L_{100} location approaches well the plasmapause when a gradient exists, which correspond to only 53% of cases during the Van Allen Probes mission. When a gradient is not defined, L_{100} reliably provides an L-shell limit for ∼85% of cases. For these reasons, readers can consider the 100 cm^{-3} density level as a proxy for the plasmapause in the present article. Note that, contrarily to this study, multiple plasmapause crossings (e.g., when the probes cross a plume) were excluded in Ripoll et al. (2022). Most plasmapause models currently used for radiation belt physics are reviewed in Ripoll et al. (2023) and plasmapause models shall not be extensively and specifically discussed here. More than the plasmapause position, we define here the *plasmapause transition region*, the region of space in which the plasma density changes from ∼30 to ∼200 cm^{-3}, whether this change occurs on a small distance when the plasmapause is a sharp gradient (decreasing exponentially with respect to L), forming a *plasmapause boundary layer* (e.g., Carpenter and Lemaire, 2004; Kotova et al., 2018) or a large distance of 0.3–1 L-shell when the plasmasphere expands and spreads smoothly (e.g., Figures 2h–2i in Ripoll et al. (2022)).

Wave particle interactions always occur within an ambient plasma, and the density influences the efficiency of those interactions. Plasma density is one important parameter inputted to the plasma dispersion relation that ultimately defines plasma wave resonant frequencies (e.g., Glauert and Horne, 2005). The resonant frequency is the frequency at which wave particle energy exchange is maximal. In the framework of quasi-linear theory, the rate of electron diffusion in energy and pitch angle is determined from resonant frequencies. The quasi-linear diffusion coefficient is evaluated at the resonant frequency for a given trapped electron, defined by its energy and pitch angle, interacting with a given wave at a given temporal and spatial location. Quasi-linear diffusion coefficients allow us to compute resonant wave particle interactions leading to pitch angle scattering, energy

diffusion, and cross energy-pitch angle diffusion, which are used in global quasi-linear Fokker-Planck simulations (see review in Ripoll et al. (2020a)). Pitch angle scattering in the plasmasphere leads, in turn, to plasmaspheric wave induced precipitation in the upper atmosphere (e.g., Imhof et al., 1986; Meredith et al., 2006). Fokker-Planck models rely thus on a firm knowledge of the plasmasphere density itself. These models also make use in general of the plasmapause position for separating whistler-mode hiss from chorus waves. Plasmapause models provided in Ripoll et al. (2022) are fully compatible with density statistics provided in this article as they are made from the same set of data (i.e., EFW s/c charging density). Variations of local plasma conditions can lead to the enhancement or suppression of the various existing waves at that location and have consequences for the precipitation of the trapped populations (e.g., Hwang and Yoon, 2018; Thaller et al., 2019). For instance, perturbation of the density by substorm activity have direct influence on wave-particle interactions (Pierrard et al., 2021c; Ripoll et al., 2020b).

In this article, we take full advantage of the high-quality and large coverage of the measurements of the NASA Van Allen Probes mission (2012–2019). We discuss the measurement techniques leading to the plasma density and present observations of the plasmasphere dynamics (Section 2). We derive new statistics of the electron density from L = 2 to L = 6, including various mean and standard deviations, with an in-depth analysis of the density variations we observe with respect to L-shell, magnetic local time (MLT), magnetic latitude, and geomagnetic conditions (Section 3). These new statistics are generated to produce models with a MLT-dependence for application in radiation belt physics and space weather codes. Main results and conclusions are compiled in Section 4.

2. Observation of the Plasmasphere by the Van Allen Probes

This study makes use of data from the NASA Van Allen Probes mission (Mauk et al., 2013). The Van Allen Probes, abbreviated RBSP, are two identical spacecraft in elliptic orbits about the Earth leading to a near-equatorial orbit with maximum excursions to MLAT ±20°. Their perigee is at ∼620 km altitude. Their apogee is near L = 6, with poor sampling in the region L > 6.5 region so that our study is geographically limited to L = 6. The probes' orbital period is ∼9 hr, and their orbits precess the Earth through all local times approximately every 2 years (see more orbit description in Figures 2a and 2b and related text). They are spin stabilized, with an ∼11 s spin. Data from the whole Van Allen Probes B mission (2012–2019) and half of the Van Allen Probes A mission (2012–2016) are used for deriving the cold plasma electron density with three different methods as described in following.

2.1. Methods to Deduce the Electron Density From Measurements

Studies on estimating the cold plasma density above the ionosphere began in the 1950's using ground-based observations of Lightning-Generated Whistlers (LGW)s, which escape Earth's ionosphere and travel along field lines in density depletions/enhancements (ducts) to a magnetically conjugate point with a frequency-dependent travel time. The dispersion characteristics can be used to estimate the cold plasma density along the field line. Carpenter and Smith (1964) compared equatorial plasma density estimates made in this way. The following sections review the main methods that have been used for deducing the plasma density from the Van Allen Probes mission.

2.1.1. Upper Hybrid Line Method

The upper hybrid resonance (UHR) method provides an accurate measurement of the plasma frequency through

$$f_{pe}^2 = f_{UHR}^2 - f_{ce}^2, \tag{1}$$

where f_{pe} is the electron plasma frequency in Hz, $f_{pe} = (1/2\pi)\sqrt{(n_e e^2)/(m_e \epsilon_0)}$, f_{UHR} is the UHR frequency, and f_{ce} is the electron cyclotron frequency determined from the observations of the local magnetic field, $f_{ce} = (1/2\pi)(eB/m_e)$, B is the magnetic field strength and the constants e, m_e, and ϵ_0, are the electron charge, electron mass, and the permittivity of free space, respectively. The plasma density is then determined through

$$n_e = \left(f_{pe}/8980\right)^2, \tag{2}$$

where n_e is in cm^{-3}.

When no UHR line is observable, the lower frequency cutoff of trapped continuum radiation may be used to infer the plasma density (e.g., Kurth et al., 2015). Note, however, that this lower frequency cutoff provides only an upper limit to the local electron plasma density. We obtain the plasma density from the UHR frequency. The upper hybrid frequency is measured by the Waves instrument which is part of the Electric and Magnetic Field Instrument Suite and Integrated Science (EMFISIS) (Kletzing et al., 2013). The Waves instrument includes a High Frequency Receiver (HFR). The maximal EMFISIS frequency is 400 kHz, corresponding to a maximal density around 2,000–3,000 cm^{-3} using Equations 1 and 2. The magnetic field strength, B, is measured by the EMFISIS magnetometer. It follows that, for the density to be determined, the UHR frequency must lie within the frequency range of the wave receiver, and the resonance (or noise cutoff) must be sufficiently strong and clear to be identifiable. EMFISIS survey mode data are routinely processed to identify the frequency at which the upper hybrid resonance (UHR) occurs. The survey mode data used to identify the UHR are based on a ∼0.5 s waveform sample taken every ∼6 s. As such, the identified UHR, and corresponding plasma density, are average values within the waveform sample period, and are output every ∼6 s. The EMFISIS team has developed a semi-automated process to extract densities from the upper hybrid line (Kurth et al., 2015). A description of the HFR spectra, and impact on wave activity in identifying the upper hybrid line can be found therein. The data set is limited to altitudes above L ∼ 2, below which the densities often translate into UHR frequencies higher than the upper frequency limit of the EMFISIS HFR (∼400 kHz). This altitude is not a hard cutoff but can vary from ∼1.5 to 2.5 depending on conditions.

For the Van Allen Probes mission, Jahn et al. (2020) reported that the upper hybrid frequency-derived total plasma densities were considered to be only available for the first ∼50% of the mission, with difficulty to establish this estimation, since the process of creating these densities is not automated. We provide a better estimation of the UHR frequency line availability during the Van Allen Probes mission based on the fact that the maximum file size for the CDF's is about 600 kbytes per day and summing filesize (n)/maxfilesize for each year and divided by the number of days per year to estimate the percentage of data availability. We find that the mean percent of available density over the 7 years is 80% for RBSP A and 85% for RBSP B. The minimum mean annual coverage is 62% for RBSP A for the year 2016 and 73% for RBSP B for the year 2014. The maximum mean annual coverage per year is 92% for RBSP A in 2015 as well as for RBSP B in 2017. It should be noted that these statistics ignore data near periapsis where digitalization is impossible due to the local f_{UHR} frequency being higher than the upper limit of the range of frequencies observed by the EMFISIS HFR. As such, these numbers are percent of possible times, not percent of all times.

2.1.2. Spacecraft-Charging Electron Plasma Density

A second way in which the cold plasma densities are determined by the Van Allen Probes is by using the spacecraft (s/c) floating potential measured by the Electric Field and Waves (EFW) instrument (Wygant et al., 2013). What we here refer to as "spacecraft potential" is a proxy of, but not equivalent to the spacecraft floating potential with respect to the ambient plasma. Rather, it is the average of opposite pairs of the single ended potentials. The single ended potentials are the sensor potential with respect to the spacecraft. For a given sensor, the single ended measurement, V_1, is $V_1 = V_1' - V_{sc}$, where V_1' is the probe potential with respect to the ambient plasma and V_{sc} is the actual spacecraft floating potential. What we are calling "spacecraft potential," V_{sc}*, is determined as $V_{sc}* = (V_1 + V_2)/2 = (V_1' + V_2')/2 - V_{sc}$ (e.g., Breneman et al., 2022). Since the potential drop between the EFW sensor is the sheath impedance times the current through the sheath (e.g., Mozer 2016), this turns out to be roughly equal to the temperature of the photoelectrons expressed in Volts, V_{ph}, so that $V_{sc}* = V_{ph} - V_{sc}$. The quantity that we are calling "spacecraft potential" is thus the negative of the spacecraft floating potential, offset by an amount equal to the sensor photo electron temperature. In the following discussion, V_{sc}* will be referred to as the "spacecraft potential." Below, we describe the fits between the spacecraft potential and plasma density. The implicit dependence that V_{sc}* has on the photoelectron temperature is thus handled by the coefficient values found by the fitting process.

The spacecraft floating potential has a density dependence because it is the potential at which the plasma thermal current, which is directly proportional to the plasma density, balances the photoemission current, resulting in net zero current to the spacecraft. The potential difference between the double probe sensor and the spacecraft is also related to the plasma density as was demonstrated using the GOES 1 and GOES 2 and

ISEE 1 missions by Pedersen et al. (1984). The functional form relating the plasma density and potential difference between the sensor and spacecraft potential is the sum of two exponential terms (e.g., Escoubet et al., 1997). Escoubet et al. (1997) used densities 100 cm^{-3} and lower for which the spacecraft potential with respect to the ambient plasma is typically positive. For the Van Allen Probes missions, the feasibility of extracting plasma density from spacecraft potential is demonstrated by Wygant et al. (2013) (see their Figure 6). Discussion on the functional relation between the ambient plasma density and the spacecraft potential can be found in Escoubet et al. (1997) and in Torkar et al. (2019). The functional form relating the density to the spacecraft potential is:

$$n_e = n_{01} e^{-V^*_{sc}/V_{f1}} + n_{02} e^{-V^*_{sc}/V_{f2}} \quad (3)$$

where n_{01}, n_{02}, V_{f1}, V_{f2} are fit parameters. In order to determine the four parameters, n_{01}, n_{02}, V_{f1}, V_{f2}, fits need to be periodically performed between the spacecraft potential and ambient density extracted from the upper hybrid frequency, f_{UHR}. From the Van Allen Probes, fits to Equation 3 have been found to work well over a range of densities 10 cm^{-3} to 3,000 cm^{-3} (e.g., Jahn et al., 2020).

The technique used to periodically determine the four coefficients is as follows. Three consecutive days per month, each month throughout the mission, are identified during which the upper hybrid line can be visually identified in the HFR spectra. Three days comprise eight Van Allen Probes' orbits. From this interval, we select ∼400–600 points using a routine in which the user visually locates the upper hybrid line and selects it, capturing the frequency, time, and concurrent spacecraft potential and magnetic field strength values. From these values, Equation 1 is used to determine the density from the upper hybrid frequency. The densities so derived along with the corresponding spacecraft potentials are fitted to a function of the form of Equation 3 with a non-linear least squares fit to determine the four coefficients. The resulting fits typically have a R^2 in the range of ∼0.75–0.95 and an average percent error between the selected fit derived densities and the densities used to perform the fit of ∼15%. The four coefficients from the fits are then used to determine the ambient plasma density from the spacecraft potential alone for intervals of ∼±2 weeks centered on the days used to determine the corresponding fit. The adequate fitting cadence was determined through experimentation throughout the first couple years of the mission. The resulting densities are stored in the Level 3 data CDF files available at the EFW web site hosted by the University of Minnesota and on NASA GSFC CDA Web. The EFW plasma density from the spacecraft potential is outputted each 33 s (three spin periods). This choice is dictated by controlling the data file size and having sufficient resolution for most purposes. ∼33 s with the orbital speed at perigee of ∼10 km/s corresponds to a distance of ∼330 km, or 0.05 RE.

The spacecraft-charging electron plasma densities are most reliable within a range between ∼10 cm^{-3} and 3,000 cm^{-3}. The upper limit of this range is set by the upper frequency of the EMFISIS HFR spectra, which is ∼400 kHz. This frequency corresponds to a plasma density of ∼3,000 cm^{-3}, ignoring the contribution of the electron cyclotron frequency to the upper hybrid frequency. Thus, while at low enough spacecraft potentials the fits do return plasma densities with values larger than 3,000 cm^{-3}, because the fits used are calibrated against the upper hybrid line, the fit quality cannot be directly verified at these larger densities. The general lower limit of ∼10 cm^{-3} is one of prudence. Experiments with individual orbits show that fits of the functional form in Equation 3 can capture the density voltage relation over a range of densities from ∼few cm^{-3} up to 3,000 cm^{-3} with the lower densities still agreeing with the EMFISIS data to within 10%. We note that the spectral resolution of the EMFISIS instrument translates to a density resolution of $\Delta n/n$ of about 10%, more likely 10%–20% (Kletzing et al., 2013). However, using the same fit for a longer period (larger than an orbit), the EFW and EMFISIS densities may diverge by over factor of two at densities <10 cm^{-3}. The reason for this is the variability of the plasma environment outside the plasmasphere, specifically the variability in the electron temperature. To use EFW densities lower than 10 cm^{-3}, they should first be used to calculate the upper hybrid frequency which is to be then compared with either the upper hybrid line or the lower frequency cut-off of continuum radiation in the HFR spectra (see Kurth et al., 2015).

As indicated above, the plasma density can be found from just the magnetic field strength and upper hybrid resonance frequency. There are thus two Van Allen Probes data products reporting the ambient plasma density: the EMFISIS teams' densities directly extracted from the upper hybrid frequency, and the EFW densities determined from the spacecraft potential and fits calibrated against densities extracted from the upper hybrid

frequencies. For periods during which the upper hybrid line is clearly resolved in the HFR spectral data, the EMFISIS density product is generally more accurate than the EFW. However, during times in which there are high levels of wave activity that make identification of the upper hybrid line difficult or impossible, resulting in increased uncertainty in the EMFISIS densities, the EFW density fits still return densities using the spacecraft potential. The derived density fits can be used with spacecraft potentials at cadences of 16 samples per second for high resolution density as well. The EFW results are invalid during periods in which the spacecraft are in eclipse and when strong storms lead to intervals of spacecraft charging. Radiation damage to the EFW sensor pre-amplifiers can also result in spurious density measurements. This particularly affected RBSP A for which caution must be exercised in data selection after April 2016. Comparisons of the statistics of the EFW densities with EMFISIS densities are provided and discussed in Section 2.3.

In this article, most statistics will be established using EFW densities. This is primarily because the EFW data set is more continuous in time since it uses regularly acquired charging measurements and a model translating these measurements to densities that is based on the empirical relation between the UHR density and spacecraft charging. This means the EFW data set does not rely onto the interpretation of every measurement to obtain a density. Once the monthly empirical relations are established, the process to obtain density from the EFW data is relatively more automatic than interpreting every HFR spectrum.

2.1.3. From Plasmaspheric Waves

A technique has been developed to estimate the cold plasma density using in situ observations of plasmaspheric hiss waves (Hartley et al., 2018b), which is of particular use at low L. This method relies on the presence of hiss waves, which are ubiquitous in the plasmasphere (e.g., Hartley et al., 2018a; Malaspina et al., 2016), and so we call it the "hiss-inferred density method" or the "hiss method." The method couples cold plasma theory, which applies well within the cold plasmasphere (few eV core electron distribution), with observations of both the electric (E^2) and magnetic (B^2) field wave power, with the plasma frequency, f_{pe} obtained through

$$B^2 = \frac{1}{c^2}\left(1 - \frac{f_{pe}^2}{f(f - f_{ce})}\right)E^2, \tag{4}$$

for a wave with frequency, f, under the assumption that the waves propagate parallel to the background magnetic field (which has shown to be a valid assumption under most circumstances for hiss waves). The plasma density is then obtained through Equation 2. A plasma density value is obtained for each of the frequency channels of the EMFISIS Waveform Receiver (WFR) instrument (Kletzing et al., 2013) where hiss is identified at each time instance. These density values are then statistically calibrated against the UHR method. The median of the calibrated densities across frequency is produced for each 6-s window, and those values are averaged over one-minute intervals for further use.

The calibrated densities from the hiss method are found to agree with the UHR densities most of the time (~<50% error in Figure 4 of Hartley et al., 2018a) over the density range 100–3,000/cm^3. Further validation with Arase density data (e.g., Hartley et al., 2023) has also been performed, with slight updates to the statistical calibration, particularly for densities greater than ~3,000 cm^{-3}. These hiss-inferred densities are typically available down to lower L shells than the UHR method, as they are not subject to the same instrumental upper frequency limit. The densities derived using the hiss method are available more than 50% of the time for $1 < L < 2$ whereas the densities derived using the UHR method are available only 10%–20% of the time in this L-shell range, and may dramatically underestimate the density in this region (Hartley et al., 2018b).

Figure 1 illustrates the wave environment and the computation of the density from the 3 methods previously discussed. There is good overall agreement among the 3 densities and we can also note some differences, which remain minor. Abrupt dips in EFW density we see for instance on 2015-07-23 ear 03:00 hr are likely due to Earth shadow since it occurs at low L and MLT near midnight.

Alternatives to these techniques are also based on wave measurements (Décréau et al., 2001; Kougblénou et al., 2011; Lointier et al., 2013; Trotignon et al., 2001) and have not been yet applied to the Van Allen Probes data. Further deduction of the plasma density from ground-based measurements of whistler data

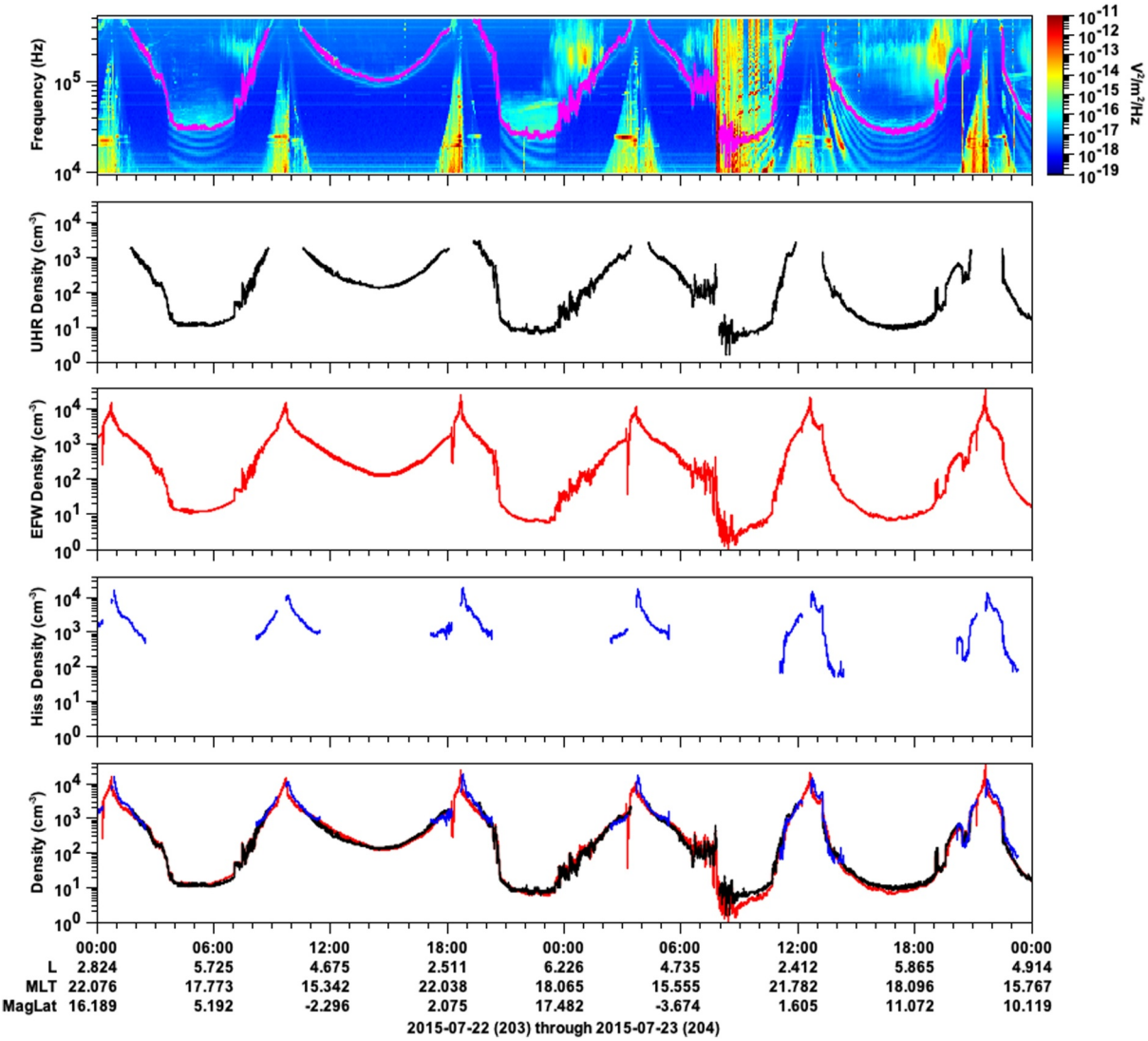

Figure 1. Overview of Van Allen Probe A observations of plasma waves and density from 22 July 2015 to 23 July 2015 (top to bottom) electric field wave power spectrogram (E2) with the upper hybrid line (UHR) line in pink, density from the UHR (cf. Section 2.1.1), density from the spacecraft charging method (cf. Section 2.1.2), and density calculated from plasmaspheric hiss (cf. Section 2.1.3). Magnetic local time, latitude, and L-shell of Probe A are given. The overall good agreement among the methods and departures of the solutions at the lowest/highest densities is shown in the last panel.

(Lichtenberger, 2009) is of high interest in practice and could be validated or/and calibrated using the Van Allen Probes data.

2.2. Spacecraft Charging EFW Electron Plasma Density in 2012–2019

The electron density is generated from RBSP-B/EFW, which has the most data, from 26 September 2012 to 16 July 2019 and shown in Figures 2c–2e. This represents the whole Van Allen Probes B mission. All measured densities are also averaged into 0.1 L bins.

The L-shell binning corresponds to a fine L-shell resolution for radiation belt studies (e.g., Li et al., 2014; Ripoll et al., 2017) and averages finer scale density structures (see discussion in Ripoll et al., 2022). A $\log_{10}$ scale is used here in order to distinguish the plasmapause transition region (~30–200 cm^{-3}) that extends far in L-shell. Both the sunspot number and the MLT coverage of RBSP-B are also represented as they directly affect the density (Figures 2a and 2b). The quieter solar activity after 2016 (Figure 2b) caused less activity and storms, which in turn disrupted less the interior of the magnetosphere, though this is not easily discerned on the plasma density of

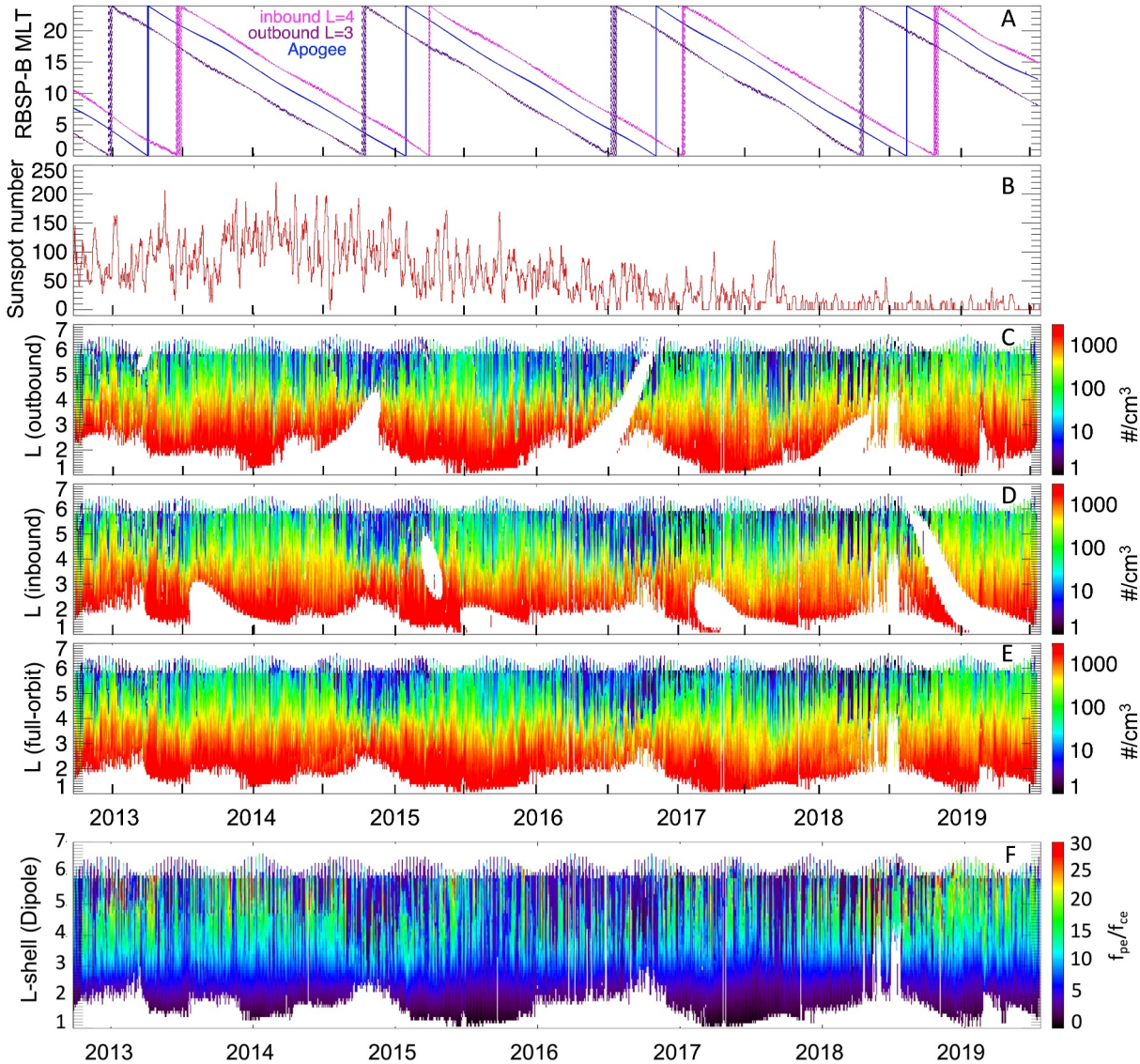

Figure 2. (a) Magnetic local time of Van Allen Probe B from 26 September 2012 to 16 July 2019. (b) Sunspot number during Probe B mission. (to bottom) The cold plasma electron density ($\log_{10}$ in cm^{-3}) deduced from spacecraft charging (EFW, Probe B). Density is plotted for (c) the outbound path only, (d) the inbound path only, (e) and both paths averaged together. (f) Ratio f_{pe}/f_{ce} of the electron plasma frequency with the local electron cyclotron gyro-frequency for both paths averaged together.

Figure 2. We also represent the inbound and outbound paths separately in order to show how data are excluded due to eclipse periods with the EFW method (cf. Section 2.1.2). As the precession of the orbit's line of apsides carries the probe across the night side, the eclipse starts first to affect the low L part of the orbit, and the effect then extends to higher L, but typically, not all the way to L = 6, but closer to L = 4, as we observe. When the satellites are in eclipse, the behavior of the potential is different, the lack of photoelectrons results in the spacecraft charging to a negative potential and the expression for current equilibrium is dominated by different terms (see more in Kotova et al., 2014). As the fit algorithm is based on the assumption of a positive spacecraft potential with photocurrent being significant, in shadow the fit algorithm does not work. Hence, the data are excluded from those regions. The averaging of both paths avoids this artificial complexity. This method is currently retained (for density and wave properties) in the event-driven Fokker-Planck simulations of Ripoll et al. (2016, 2017, 2019, 2020b, 2020c).

The ratio of the electron plasma frequency ($f_{pe} = \omega_{pe}/2\pi$) with the electron cyclotron gyro-frequency ($f_{ce} = \omega_{ce}/2\pi$) computed from the local measured magnetic field is shown in Figure 2f. Lacking data below L = 1.8 indicates

the upper hybrid line is at too high frequency to be measured by EMFISIS so that EFW spacecraft charging density cannot be calibrated. Daily variations due to geomagnetic activity are well shown. The f_{pe}/f_{ce} ratio is generally below 10 for L < 2.5. Above L = 3.5, variability of f_{pe}/f_{ce} is maximal, varying between ∼5 and ∼30. High ratios are more often seen in the 2013 and 2014 years, for which activity was the strongest (cf. sunspot number in Figure 2a). The plasmasphere is also less spread in L-shell on the night side (around March 2013 and July 2016), which will be confirmed in the statistics of Section 3. Variations shown in Figure 2f are complex and can be further explained by sorting with MLT (cf. Section 3 and Figure 5).

2.3. Statistical Validation of the Spacecraft Charging EFW Density

The study of Jahn et al. (2020) is dedicated to establishing how the density obtained by the EMFISIS upper hybrid resonance and the density obtained from EFW spacecraft charging compare. Using 3.5 years of Van Allen Probes data, Jahn et al. (2020) found that, statistically, the ratio of EFW to EMFISIS densities are mainly distributed within a factor of 2 about a ratio of 1 from ∼10 to 20 cm^{-3} to 3,000 cm^{-3}, and that the distribution is strongly peaked about a ratio of 1 (see Figure 4 in Jahn et al. (2020)). Figure 2 of Ripoll et al. (2022) compares 14,907 plasmapause positions obtained from both methods, whether the plasmapause is computed by a gradient or a density level. Distributions with respect of L-shell, MLT, density, plasmapause location are established systematically for both EFW (spacecraft charging) and EMFISIS (f_{UHR}) densities showing good concordance (see also Figures S1 and S3 in Supporting Information of Ripoll et al., 2022). In the following sections, we provide further direct comparison of spacecraft charging and f_{UHR} based densities with the computation of their relative error and further convert the error made in electron density in a L-shell variation.

2.3.1. Comparison With Density Derived From the Upper Hybrid Resonance

EMFISIS f_{UH} based electron density has been generated for RBSP-A from September 2012 to April 2016 for 4 Kp bins and is used here as the reference density to establish the variability and robustness of the statistics of EFW electron plasma density, previously shown. Both sets of density are binned in 4 bins of magnetic local time, 60 bins of L-shells, and 4 bins of geomagnetic activity (similarly to what is done and explained in Section 3). The validation is performed bin by bin (for 4.91×10^6 values when binned by Kp and Dst and for 3.96×10^6 values when binned by AE), rather than for single measurements as performed in Jahn et al., 2020, since this binning used for the models we develop in Section 3.

The top panel of Figure 3 shows the percent error of the EFW density relative to the more accurate EMFISIS upper hybrid frequency density, $100 \times (n_{UHR} - n_{EFW})/n_{UHR}$. The error between the EFW and EMFISIS density values is found and binned by L values and Kp. The percent difference is bounded by ±20% for quiet and moderate activity (Kp < 5) when all MLTs are averaged together. For stronger activity, mean differences can reach up to ±30% for Kp < 7. These agreements are particularly good. On the contrary, for extreme events (Kp > 7), the mean error is ±100%. In all cases, the difference is the largest at the highest L-shells for the lowest densities. Looking at MLT bins, the dawn and night sectors have the highest difference (omitting the Kp > 7 bin which error is equally high unless when missing in the dawn sector).

In Figure 3(top), the error bars show the standard deviation of the error in each bin. For Kp < 7, the many points lead to good statistics, with error bars confined tightly around the points and errors bounded by ∼10%. For Kp > 7, there are fewer points, though enough to see that the difference between the two densities is higher for those more active times. Errors can reach ∼50% between L = 3 and L = 5, a region in which strong storms cause the position of the plasmapause and of the last closed L-shell to be. Errors can be due to greater difficulty in picking out the upper hybrid line during active times since other features appear in the spectra as well as the s/c charging method reaching its lower density limit. In the latter case, we believe spacecraft charging density should be accurate for very low densities in the absence of energetic particle fluxes.

2.3.2. Conversion of Density Errors Into L-Shell Errors

We measure a variation in L-shell between the L-shell of the density from EFW and the closest L-shell at which the f_{UHR} reference density is found with the same density to find how much a mean percent difference in density represents in variation in L-shell. This way we convert a possible error caused by the s/c charging density (in comparison with the f_{UHR} based electron density) into a L-shell error. Such a L-shell error can potentially be associated with the misplacement of whistler-mode waves (e.g., Malaspina et al., 2016, 2018). This is useful for

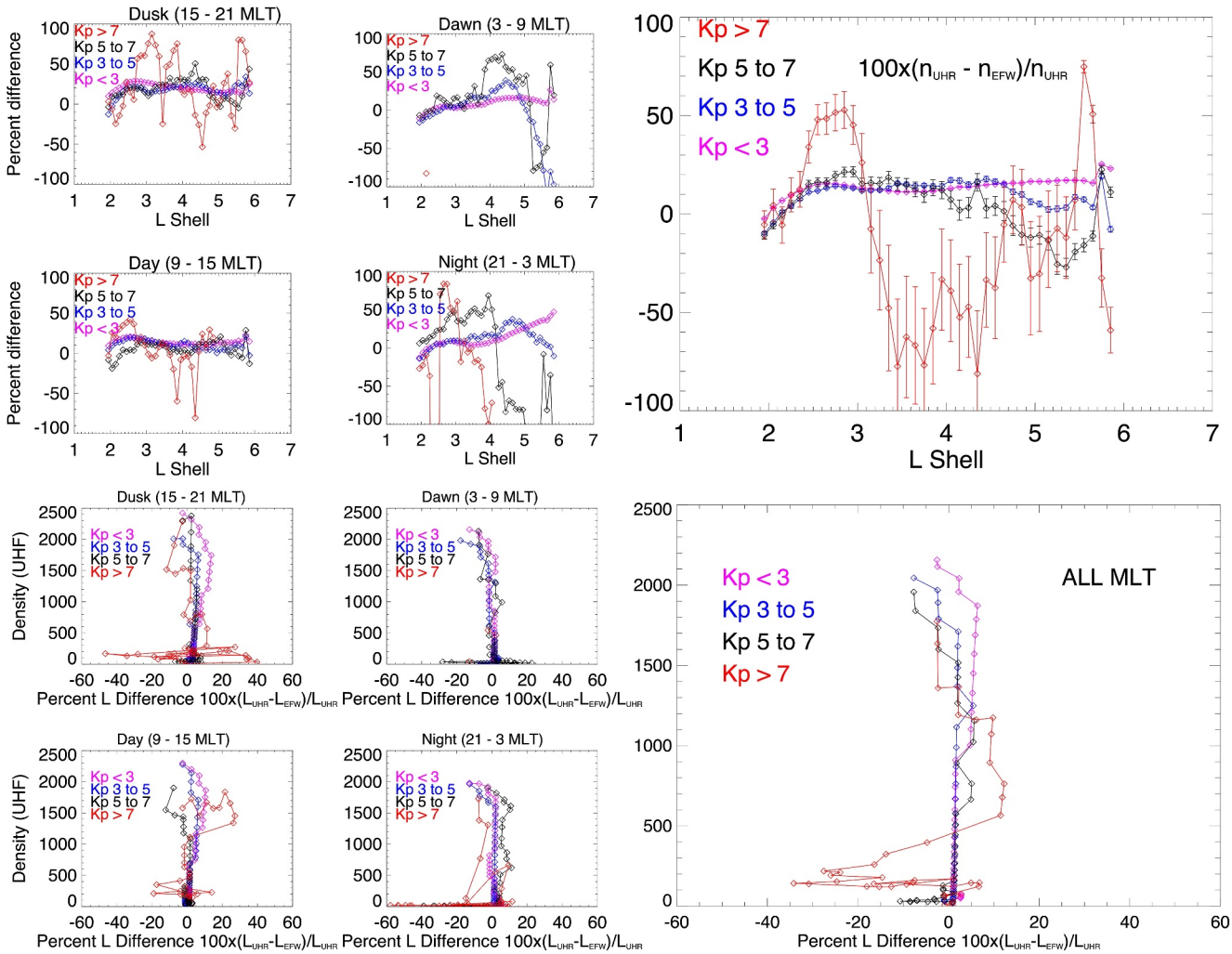

Figure 3. Comparison of the s/c charging (RBSP-A/EFW) density with the f_{UHL} based (RBSP-A/EMFISIS) electron plasma density statistics at different MLT sectors (dawn/day/dusk/night) and sorted by Kp index. (top) The mean percent difference, $100 \times (n_{UHR} - n_{EFW})/n_{UHR}$, between the two densities versus L-shell. (bottom) The mean percent L-shell difference, $100 \times (L_{UHR} - L_{EFW})/L_{UHR}$, representing the equivalence between the variation of the density and a variation in L-shell for a given UHF density level.

radiation belts physics for which reaching an accuracy of ~0.25 L-shell is already a good achievement. Figure 3 (bottom) shows the mean percent L-shell difference, $100\times(L(n_{UHR})-L(n_{EFW}))/L(n_{UHR})$, noted $100 \times (L_{UHR} - L_{EFW})/L_{UHR}$, needed to produce an equivalence between the variation of the density and a variation in L-shell. This is computed using the mean EFW and UHR densities per bin with 0.1 L resolution every four hours (half orbit). For instance, the 10% variation of the mean 50 cm^{-3} level for Kp in (5,7) in Figure 3 (bottom, right) represents a ~0.5 L difference at L ~ 5. The latter assessment requires the knowledge of the mean density which will be presented and discussed in Section 3 and Figure 8. According to Figure 8, we can read the mean 50 cm^{-3} level for Kp in (5,7) is at L ~ 5.

Figure 3(bottom) confirms the excellent agreement found previously, with the percent L-shell difference under ±12% (omitting the Kp > 7 bin). The large difference above 50% at L ~ 4 in the dawn sector for Kp in (5,7) is associated with the plasmapause transition region, more specifically with the density of n_e ~ 100–200 cm^{-3} at L = 4 (see Figure 8 at L = 4 for Kp in (5,7)). Both correspond to the large variation in L-shell by −30% to +20%, that is, an error of ~1 L. The 45% L difference in the dusk sector for Kp > 7 corresponding to ~200 cm^{-3}, in the plasmapause vicinity, represents this time an error of ~1.5 L. This also demonstrates the large variability of the properties for extreme events, which necessarily has a strong impact on the accuracy of their prediction. For instance, it can cause a significant error in misplacing a chorus wave model by ~1.5 L, which in turn will impact

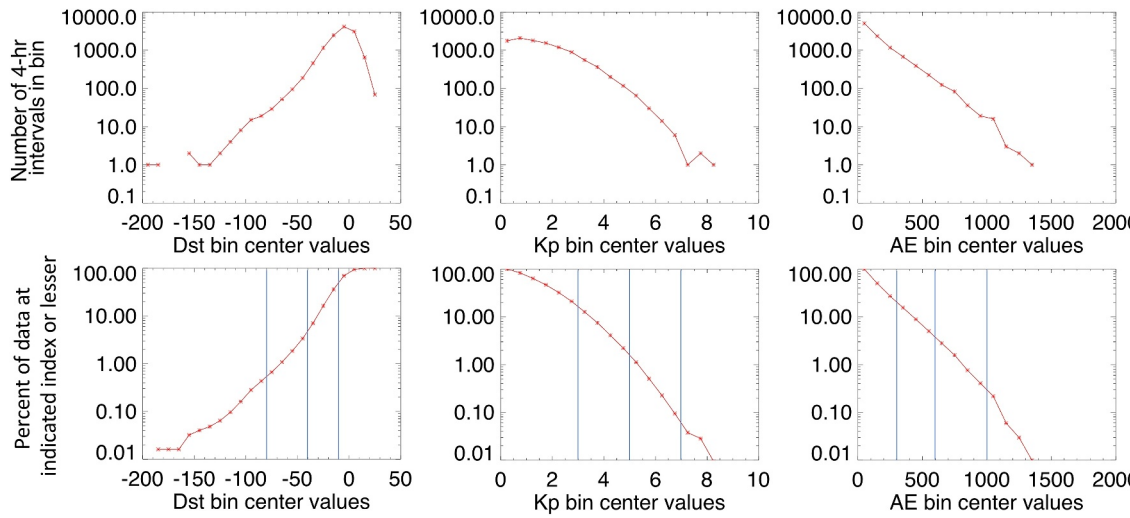

Figure 4. Statistical repartition of geomagnetic activity during the Van Allen Probes era (12/2012–07/2019) with (top) the number of 4-hr time interval with a mean (left) Dst, (center) Kp, and (right) AE. (bottom) Cumulative statistics giving the percentage of data at the indicated index or lesser (more negative for Dst) or higher (for Kp and AE). For instance, Kp < 2 represents 60% of the activity. Blue lines mark the four bins chosen for the statistics of Section 3.3 based on commonly used ranges in radiation belt codes.

the local acceleration caused by this type of storm. The largest errors are found below ∼200 cm^{-3} in the plasmapause transition region, which indicates that this region should be investigated more. It is also interesting to note that the statistical error can compensate in MLT due to the MLT bin size showing that a difficulty is to capture the correct drift of the plasma density. Current radiation belt modeling approaches increasingly need to incorporate MLT variations to account for the specific location of whistler waves, such as chorus waves in the dawn sector (e.g., Meredith et al., 2012). Accurate modeling requires a synchronization between the MLT variation of the density and the MLT variation of the whistler wave system in order to perform self-consistent wave-particle interactions. Today, the use of MLT-averaged densities and MLT-averaged wave properties in most radiation belt studies prohibits this improvement.

3. Van Allen Probes Statistics of the Electron Density for Radiation Belt Physics

3.1. Variability of the Geomagnetic Conditions During the Van Allen Probes Era

The evolution of the plasmasphere and the radiation belts is controlled by the solar wind activity, the magnetic field deformation and fluctuation, the incoming substorm injections, etc, all represented by various indices that in turn are often used as parameters for the various models, here for the empirical modeling of density. The Bartels Kp index is commonly used for statistical density and wave models (e.g., Pierrard et al., 2021b). The Auroral Electrojet AE index is also often used for wave models. Quasi-linear diffusion coefficients using these models need thus a similar parametrization of the density with respect to the Kp or AE index. The Disturbed Storm Time Dst (or Sym-H for a higher time resolution) index is commonly used for quantifying storm evolution as well as the plasmasphere (e.g., O'Brien and Moldwin, 2003). Before binning by Kp, AE, Dst as done in the next section, it is thus interesting to start by looking at the distribution of these three indices to understand which density data will be the most or the least represented in a given index bin. For instance, improving the accuracy of the most frequent bins helps to reduce repeated errors and limit model deviation.

From now on, geomagnetic indices are binned into 4-hr bins, that is, the lowest temporal resolution retained in Section 2.3 allowing the coverage of all the L-shells of half an orbit. The 4-hr averaging we use has the caveat to diminish extreme indices (compared with no averaging) but does not change the statistics presented in the following.

Figure 4 shows the statistics of the geomagnetic activity during the whole Van Allen Probes era generated from indices. Looking at low geomagnetic activity with Kp < 2, it represents ∼60% of all times of the Van Allen Probes. This corresponds to AE<200 or Dst > −20 nT. We note 90% of the activity has a Kp index lower than 3.5, Dst index above −30, and AE below 420, which represent quiet to moderately low activity. The one percent of the

total activity corresponding to intense geomagnetic activity occurs for Kp > 5, Dst < −65, and AE > 820 during Van Allen era. Extreme events with a 0.1% realization rate have Kp > 7, Dst < −120, and AE > 1100. These statistics lead to a few conclusions: storms are such rare events that their statistical description is necessarily limited and requires many years of observation. They create intense and global effects such as orders of magnitude flux enhancements and/or dropout throughout the belts, which in turn have longer time scale effects occurring during mild to quiet activity. They thus remain important even if representing about one percent of the statistics. On the contrary, quiet and moderate activity intervals benefit from large statistical coverage, though we will see there is still a large variability of the plasmasphere above Kp = 3 (cf. Section 3.3). Quiet and moderately low activity times represent the surrounding and ambient environment of the belts in 90% of the cases, whether or not the belts have been disturbed by intense or extreme events.

The three vertical lines in Figure 4(bottom) separate the 4 macroscopic bins of activity that we define and use below for the density statistics. It should be noticed that the bins are not in concordance with each other in terms of percent of data they represent, particularly for the most active times. For instance, for the extreme condition bin, the Kp > 7 bin represents ∼0.05% of the events while the AE > 1000 bin and the Dst < −80 represents in turn ∼0.5% of the events. Comparisons between index bins must be made carefully.

3.2. Statistics of the Electron Plasma Density

In the following sections, the EFW density for the whole Van Allen Probes B era (cf. Figure 2) is discussed and used for generating the various statistics. The EFW density has been divided in bins of magnetic local time, L-shells (with a 0.1 L resolution), and index of geomagnetic activity. We compute both the mean density, $n_e = \sum n_{e,i}/N$ and the standard deviation, $\Delta n_e = \sqrt{\sum (n_{e,i} - n_e)^2/N}$, for $i = 1 \ldots N$ measurements in a given bin in (L, MLT, index). The mean electron plasma density is plotted versus L-shell and MLT for unitary Kp bins in Figure 5 (two top rows). The number of measurements used for the study is represented in terms of coverage in hours in small inserts in Figure 5. Time is computed by adding the number of events in a given (L, MLT, activity) bin multiplied by 33 s, which is the duration of a single measurement. They indicate that the statistics are converged up to Kp < 6. The precession period of the Van Allen Probes orbit (∼22 months) is such that ∼1 MLT is covered in ∼1 month so that the full MLT description is only possible using statistics made over years with the data of this mission. Real time MLT resolution of the plasmasphere requires multi-spacecraft observations as proposed nowadays in new mission concept (e.g., Goldstein et al., 2022; Malaspina et al., 2022).

For quiet times, the mean plasmasphere is approximately circular (when Kp < 1), with low asymmetry (starting for Kp = 1–2). The mean 100 cm^{-3} level line is above L = 5 and the 10 cm^{-3} level is above L = 6 for Kp < 1. For Kp < 2, the mean 100 cm^{-3} level line is at L = 5 on the dayside and slightly below L = 5 on the nightside, indicative of a slight asymmetry forming. Since Kp < 2 represents ∼60% of the events in Figure 4 (bottom row), this causes the electron outer radiation belt (>50 keV, centered around L ∼ 5) to be within the plasmasphere for ∼60% of all times. As soon as activity increases (Kp > 2), we see in Figure 5 this gradual asymmetry increasing with higher mean density in the afternoon sector around ∼15–16 MLT, which is associated to some detached density regions and plumes expanding outward. Mean densities are in turn much lower on the dawn and night sectors. We can find a ratio of 5–10 in density from one sector to another (to be discussed more precisely below). The mean 10 cm^{-3} level is not visible since it is located farther out the Van Allen Probes orbit during quiet times (Kp < 2) and during plume expansion on the day/dusk sector. For Kp = 5–6 and Kp = 6–7, the mean 10 cm^{-3} level on the night side (∼23 MLT) and dawn/night side (∼6 MLT) expands further. We believe this is due to higher density plasma formed by detached plasma pockets, which wrap around the Earth on the dawn and night sides between L = 4 and L = 6. This leads to a night side that is more dynamic (comparing with Kp = 3–5 conditions) and with more statistical variations in the 10 to 100 cm^{-3} region.

For times when the Van Allen Probes are in eclipse (i.e., Earth's shadow), Equation 3 is no longer valid, and the densities are not determined. Typically, eclipse conditions are experienced closer to Earth, at low L values, however, there are periods where the orbital trajectory is in shadow over a significant range in L. The effect of the Earth's optical shadow on thermal plasma measurements in the plasmasphere is discussed in Kotova et al. (2014). For Kp = 6–7, the high-density region below L ∼ 2 is now undetermined both on the night and day sides. Density plotted in (L, MLT) versus Dst are available for comparison in Figure 1 of Ripoll et al. (2022). For instance, the

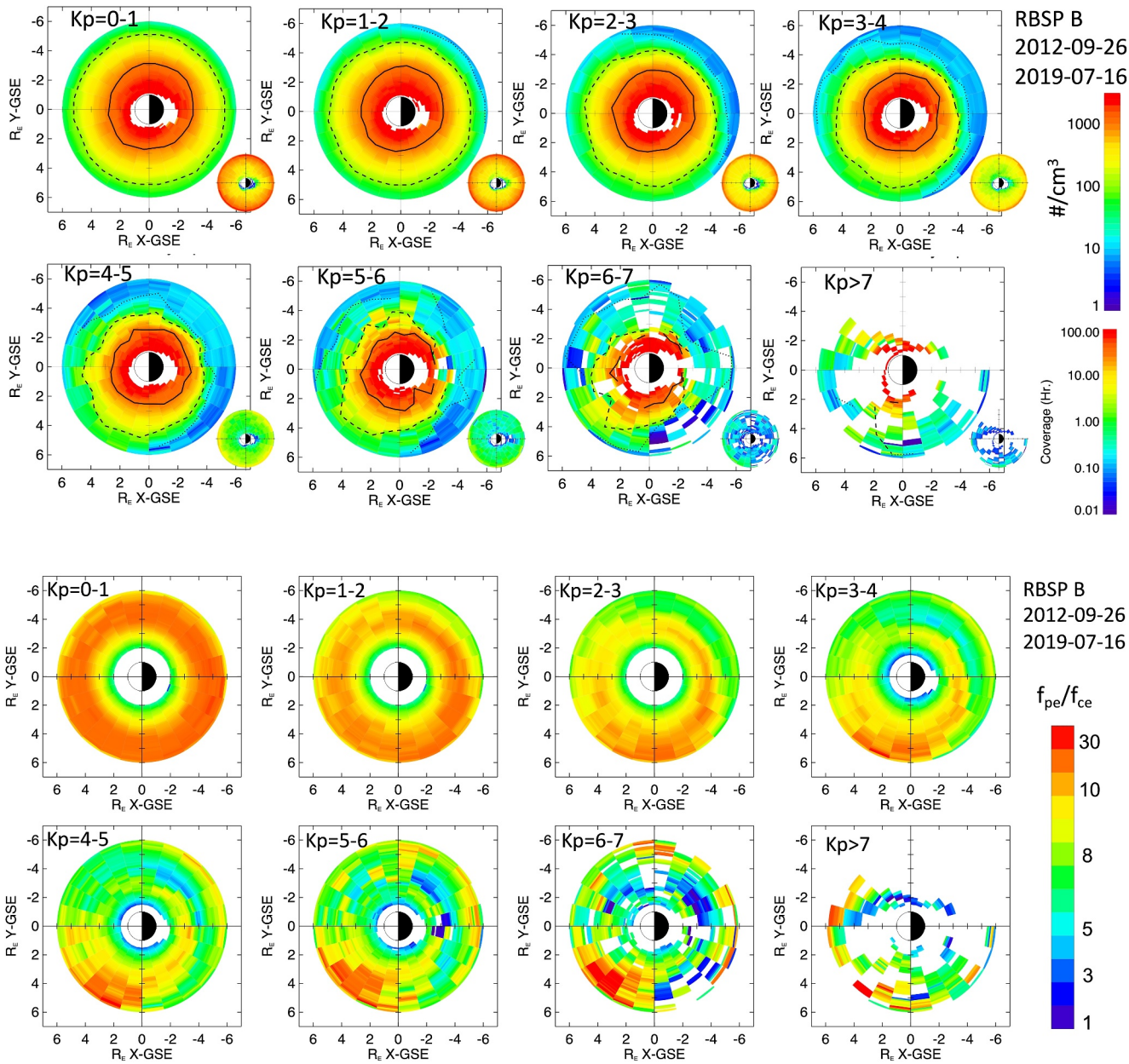

Figure 5. (two top rows) Statistics of the s/c charging EFW mean electron plasma density plotted versus L-shell and MLT for 8 Kp bins of unitary width. The (solid line) 1,000 cm^{-3}, (dashed) 100 cm^{-3}, and (dotted) 10 cm^{-3} levels are also indicated when possible (for Kp > 1, more often on the night side). Small inserts give the coverage in hours. (two bottom rows) Same for f_{pe}/f_{ce} (without level lines).

gradual asymmetry forming for Kp = 2–3 is found for Dst ~ <−15. Level lines of mean density versus MLT will be showed and discussed in Figure 9 and related text in Section 3.5.

Maps in L-value and MLT of the ratio of the average plasma frequency, f_{pe}, to the electron cyclotron frequency, f_{ce}, for different Kp levels are shown in the bottom two rows of Figure 5. The measured local magnetic field is used to evaluate f_{ce}. The f_{pe}/f_{ce} ratio is used for some formulation of the diffusion coefficients in radiation belt codes (e.g., Glauert and Horne, 2005; Reidy et al., 2021). For the quietest periods, 0–1 Kp, the distribution of the f_{pe}/f_{ce} ratio is symmetric with larger values distributed mostly for L > 4. This symmetry is due to the symmetric distribution of density in MLT, as is seen on the top row in the leftmost panel. The asymmetry of the Earth's magnetic field is not strong enough to unsymmetrize the f_{pe}/f_{ce} ratio. The lower values of the f_{pe}/f_{ce} ratios at low L values, L < 2, are due to the fact that the magnetic field rapidly increases close to Earth due to its $1/L^3$ dependence.

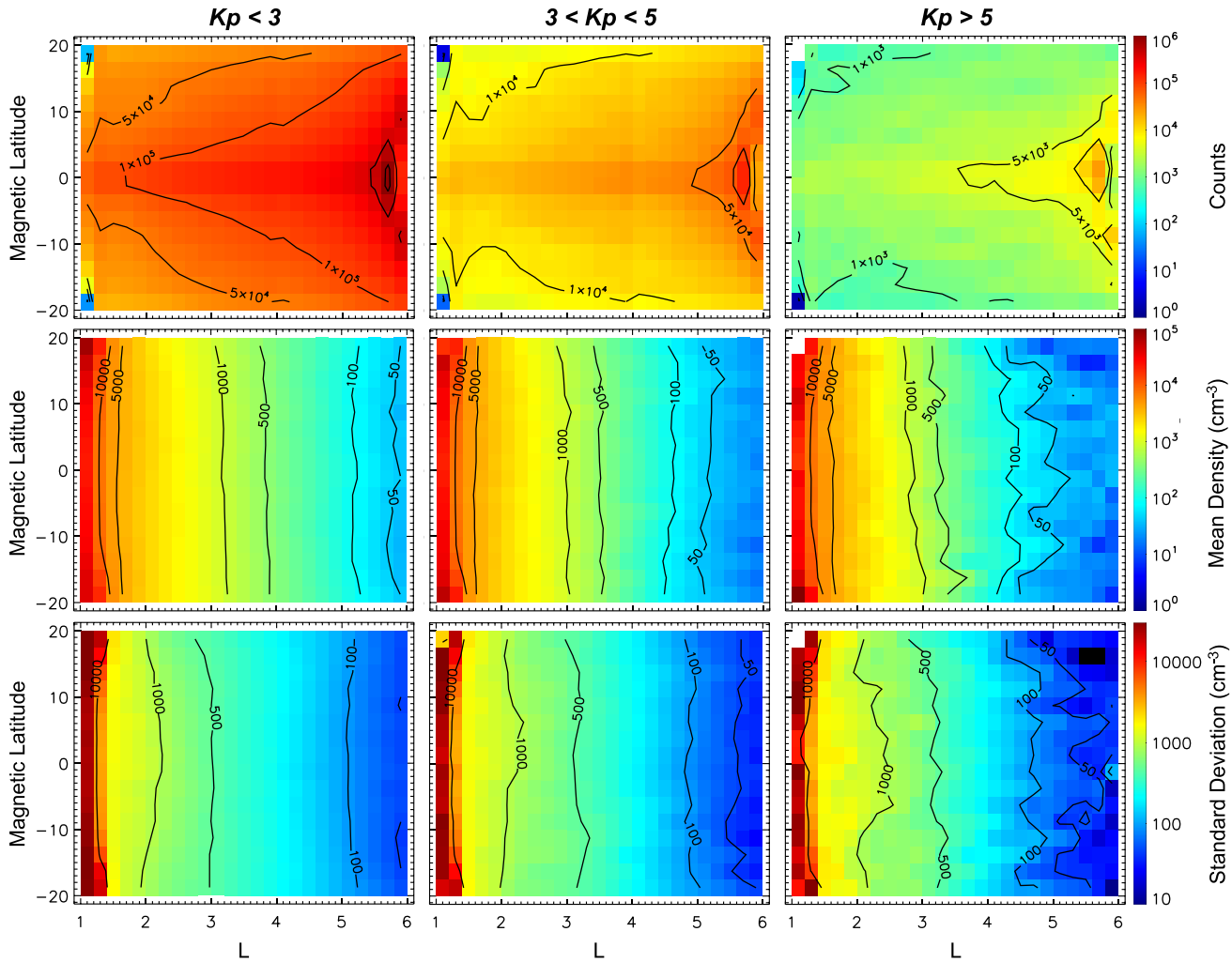

Figure 6. Latitudinal variation of the cold plasma density from RBSP-A and RBSP-B at all MLT for three Kp bins. (top) counts, (middle) mean density, (bottom) density standard deviation. Density is derived from the UHR frequency when available complemented by the density from the hiss-inferred method for L < 4.

As the geomagnetic activity increases, the plasmasphere erodes. As can be seen in the plasma density (top two rows), this erosion first appears in the post-midnight sector and works its way earthward and azimuthally east and west as the Kp index increases. This is reflected in the f_{pe}/f_{ce} as the decrease in the ratio there, progressing with a similar morphological development with increasing Kp. The remaining region of elevated density on the post-noon to dusk sector, corresponding to the drainage plume, is likewise reflected in the elevated f_{ce}/f_{pe} ratio (above 10) in the same locations. The increase in Kp has a much less noticeable effect on the magnetic field, especially at low L values. The routinely low f_{pe}/f_{ce} ratio at low L values, combined with the decreasing f_{pe}/f_{ce} ratio at higher L values, results in a complex morphology of the f_{pe}/f_{ce} distributions on the night side. In particular, for moderate Kp values, Kp = 3–4 and Kp = 4–5, there is a region for high f_{pe}/f_{ce}, starting near dawn, crossing the post-midnight sector, and merging into the dusk-side bulge region. This arc of high f_{pe}/f_{ce} is bounded radially by the low ratio due to the high magnetic field strength on the Earth side, and by the low ratio resulting from low density on the higher L side. The nightside part of the arc of high f_{pe}/f_{ce} ratio narrows with increasing Kp as the density diminishes with plasmasphere erosion. The elimination of the high f_{pe}/f_{ce} arc at Kp > 7 is obscured by lack of coverage.

3.3. Latitudinal Dependence Within ±20°

The latitudinal variation of the cold plasma density from both RBSP-A and RBSP-B is presented in Figure 6 (middle row) for all MLT, with density measurement counts (top row) and standard deviation (bottom row). We

use the density from the UHR when available and the density from the hiss-inferred method for L < 4 (e.g., Hartley et al., 2023) whenever there is no data from f_{UHR}. Three Kp bins, Kp < 3, 3 ≤ Kp < 5, and Kp ≥ 5 are defined in order to find a compromise between the (L, MLat) statistical resolution and the geomagnetic dependence. We find no significant density dependence with latitude within ±20° of magnetic latitude above L> ∼ 2. Specific statistics generated either on the night side and the day side are somewhat under-resolved due to lack of data, but do not exhibit more latitudinal variation than what is visible in Figure 6, for a lesser resolution in (L, MLat). For lower L-shells (L < 3), we refer to Hartley et al. (2023), where a full (L, MLat) density model is derived by combining Van Allen Probes and Arase data to Miyoshi et al. (2018), the latter satellite bringing higher latitude density values, which are crucial to capture this dependence. An MLT dependence was shown to primarily occur at low L-shell (L < 1.5) (originating from the LT dependence of the ionosphere) and to decrease substantially above L = 1.5 up to L = 4 (Hartley et al., 2023). For quiet time (Kp < 3), the 50 cm^{-3} level line, which can mark the plasmapause region, shows oscillations with respect to MLat for L > ∼5.5. These oscillations are amplified for density ∼100 cm^{-3} for 3 ≤ Kp < 5 above L ∼ 4.5. For Kp ≥ 5, the mean density is more perturbed and oscillating with respect to magnetic latitude above L = 2. Level lines show wiggles below 5,000 cm^{-3}. The 50 cm^{-3} level line shows a pocket structure of the density, which is ∼10° wide in latitude for L between L ∼ 4.5 and L ∼ 5. This feature is also present in the standard deviation (Figure 6, bottom row) and is not due to a too low number of events (Figure 6, center). Although, we do not find a physical law for the density dependence with latitude, the mean density does change with latitude in the plasmasphere-plasma trough transition regions, with more variation as activity increases. Because the two Van Allen Probes cover a single latitude per half orbit, it is not possible to establish whether this is a statistical effect or if the plasma dynamic or erosion is three dimensional. For comparison, the 3D neural network model of Chu et al. (2017) does not exhibit a noticeable dependence with latitude (cf. their Figure 9).

3.4. Models of Mean Electron Plasma Density With and Without MLT Dependence

The EFW mean density (presented in Figure 2) is now divided in 4 bins of magnetic local time, 60 bins of L-shells, and 4 bins of geomagnetic activity. MLT sectors are defined as dawn (03–09), day (09–15), dusk (15–21), and night (21–03). Density counts are provided separately for each MLT sector in Figure 7 (left, 2 × 2), as well as for all MLT sectors in Figure 7 (right). Different geomagnetic indices are presented in top (Dst), middle (Kp), and bottom (AE). From the statistics of geomagnetic activity (cf. Figure 4), the black (resp. red) line is associated with intense (resp. extreme) storms, representing a few percent (resp. few tenth of percent) of the events. Statistics for extreme storms are always more limited. The less resolved (red) bin in the all-MLT figure has a minimum of ∼30 values for Kp and ∼100 values for Dst and AE at L = 2. The minimum number of available values increases with L-shell (and activity) to be ∼100 for Kp and ∼1,000 values for Dst and AE for this same bin. Therefore, MLT-binned statistics of the most active bin are likely under-resolved and only plotted as an indication of the evolution caused by the strongest events. This comment applies to Figures 5, 7–10.

The EFW mean density is plotted in Figure 8 with the same format, either averaged by MLT sectors or for all MLT sectors. For the quietest activity bin, the mean 100 cm^{-3} level can reach L ∼ 6. The mean 100 cm^{-3} level can be considered at the location of the plasmapause as shown in Ripoll et al. (2022). This implies the outer electron belt lies fully within the plasmasphere for quiet times. Dusk is the least sensitive sector to activity, particularly visible when sorted by Kp, with a variation by 0.25 L for the 500 cm^{-3} level for all Kp bins but the highest (see confirmation from the standard deviation computed in Figure 10). This may be explained by the large density values due to plasmaspheric expansion during moderately to active times. For comparison, at night, the mean 500 cm^{-3} level varies by 1 L-shell (from L ∼ 2.8 to 3.8) for all Kp bins except for the highest bin. Looking at the mean 500 cm^{-3} level, the MLT-dependence is not strong, with a location close to L ∼ 3.7 (resp. L ∼ 3.9) for the quietest bin with Kp < 3 (resp. Dst > −10). Therefore, density in Figure 8 (center) can be considered to be between ∼500 and ∼50 cm^{-3} a great majority of the time between L ∼ 4 and L ∼ 6 during quiet times, with Kp < 3 events representing more than 80% of total activity (according to Figure 4).

As activity increases, the MLT variability of density becomes more pronounced, with an important day-night difference. The mean 500 cm^{-3} levels varies between L = 3.2 and L = 3.7 for Kp in (3,5) and between L = 3.3 and L = 3.6 for Dst in (−40,−10). The mean 1,000 cm^{-3} level varies between L = 2.2 and L = 3.2 from the highest to lowest Kp or Dst bin on the night side and between L = 2.2 and L = 2.8 from the highest to lowest Kp or Dst bin on the day side. Above 1,000 cm^{-3}, the largest variations due to geomagnetic activity occur in the night sector. Active time electric field enhancements do penetrate earthward of the plasmapause, so that they

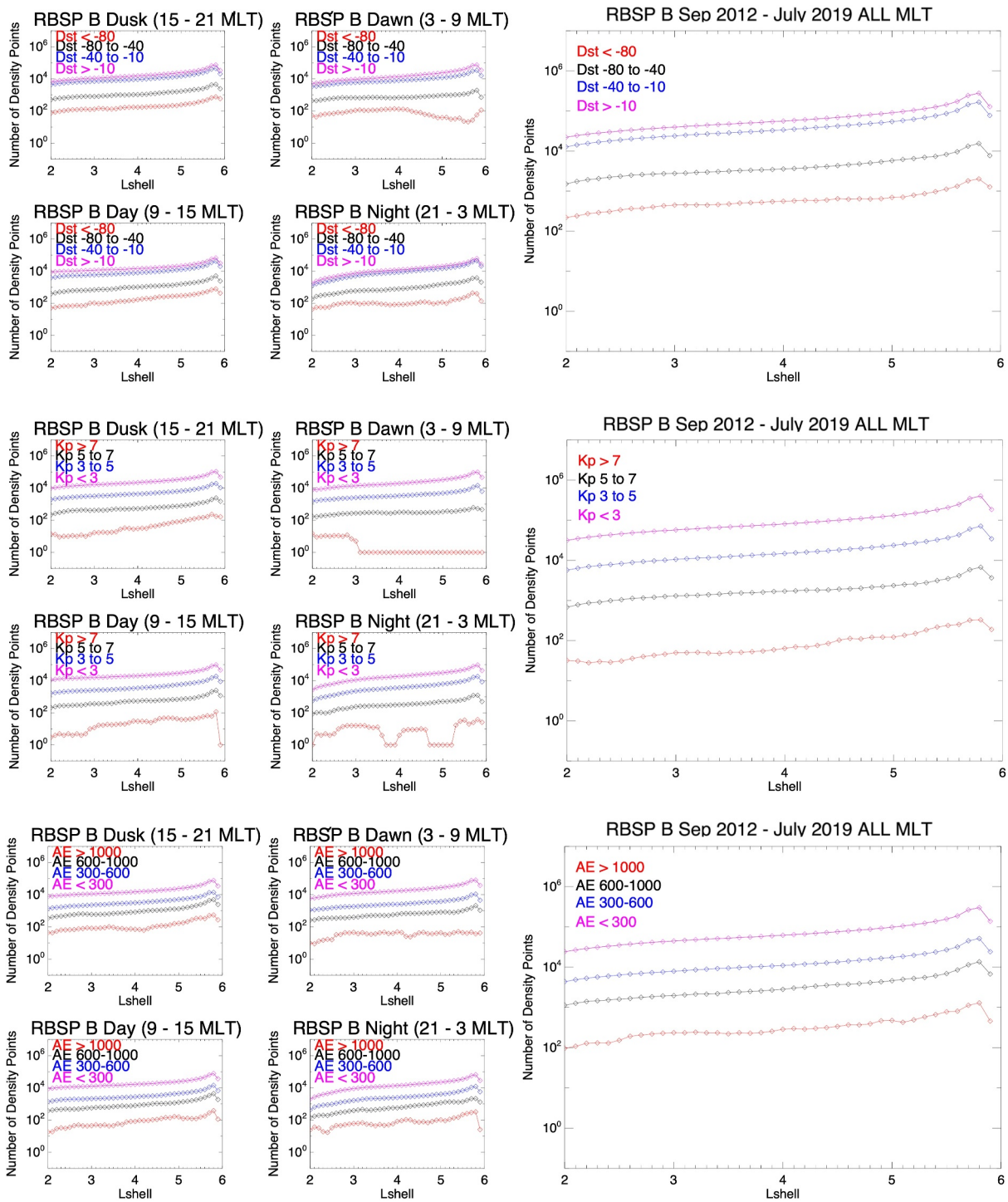

Figure 7. Counts of s/c charging EFW density values measured at 4 MLT sectors (left column the day side, 9–21 MLT, and right column the night side, 21–3 MLT, clockwise in the order of dusk/dawn/noon/midnight) (left panels) and all MLTs (right) and sorted by (top) Dst, (center) Kp, and (bottom) AE index for the whole RBSP B mission. These statistics serve in Figures 8–10.

should have an impact on the density inside the plasmapause. This is confirmed by preliminary MHD simulations showing the flow around the Earth interferes and reduces the plasmasphere (Figure 2a in Ripoll et al., 2023). This is also consistent with the physics-based Belgian SWIFF Plasmasphere Model (BSPM) model of the electron density (Pierrard et al., 2021a). There is a saturation effect of density variations with the AE index for which the two highest activity bins show a similar position with respect to L-shell, contrary to Kp and Dst. This could have

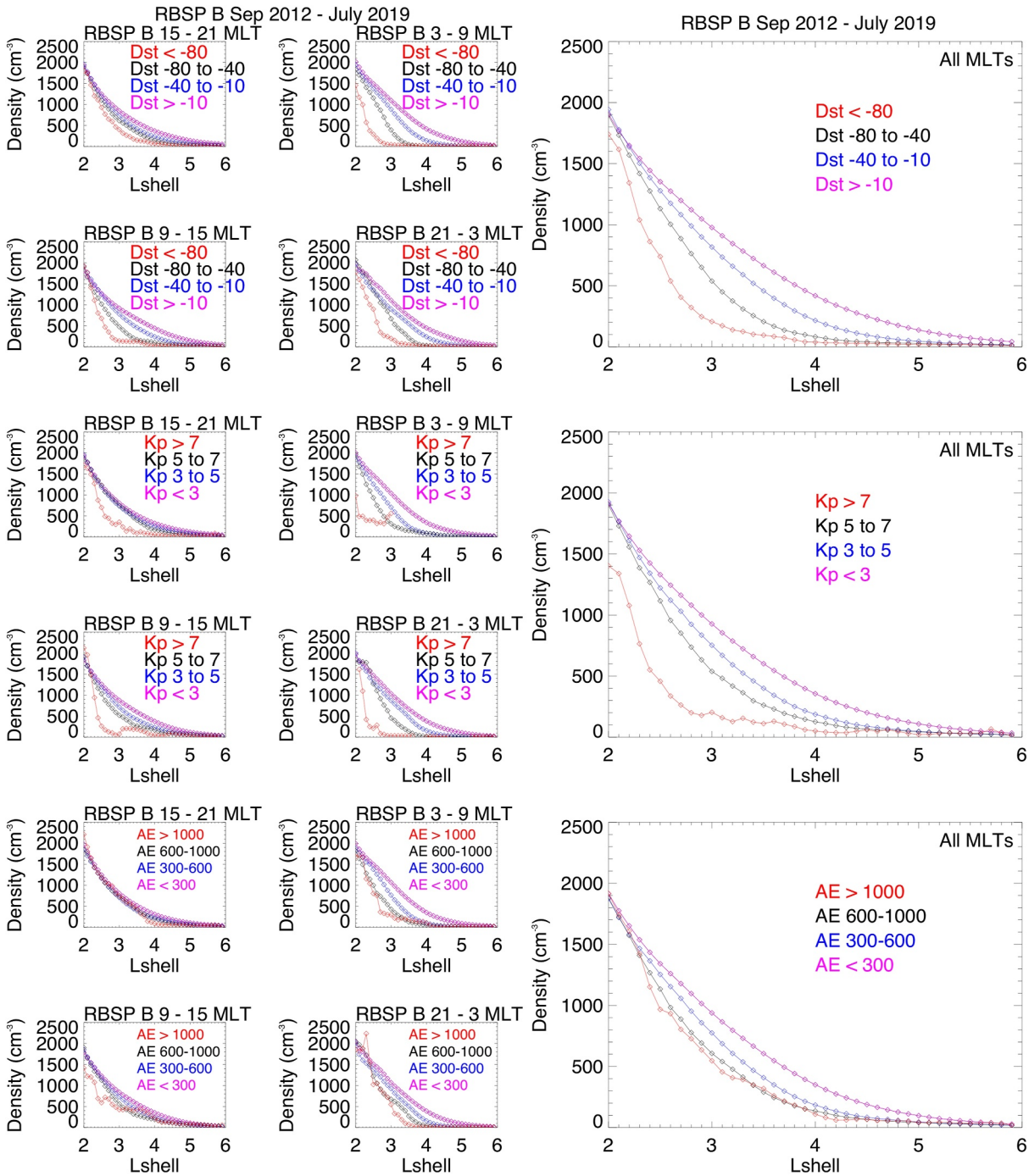

Figure 8. The s/c charging EFW sample mean electron plasma density measured at 4 MLT sectors (left column the day side, 9–21 MLT, and right column the night side, 21–3 MLT, clockwise in the order of dusk/dawn/noon/midnight) (left panels) and all MLTs (right) and sorted by (top) Dst, (center) Kp, and (bottom) AE index for the whole RBSP B mission. Fits of the mean density line plots are available in Tables 1–3.

an important implication according to whether a wave model is defined in terms of Kp or AE, as the density varies differently. There are some plume effects in the statistics on the dayside with another high-density zone outside the main dense plasma for both Kp in (5,7) and Kp > 7.

The mean densities of Figure 8 have been fitted with polynomial functions of order 2, $\log_{10}(n_e(L)) = a_0 + a_1 L + a_2 L^2$, for use in radiation belt codes. Fits for each index (Kp, Dst and AE) are reported in Tables 1–3 with their fitting error. The fitting error is computed by taking the mean of the percent difference between the fit

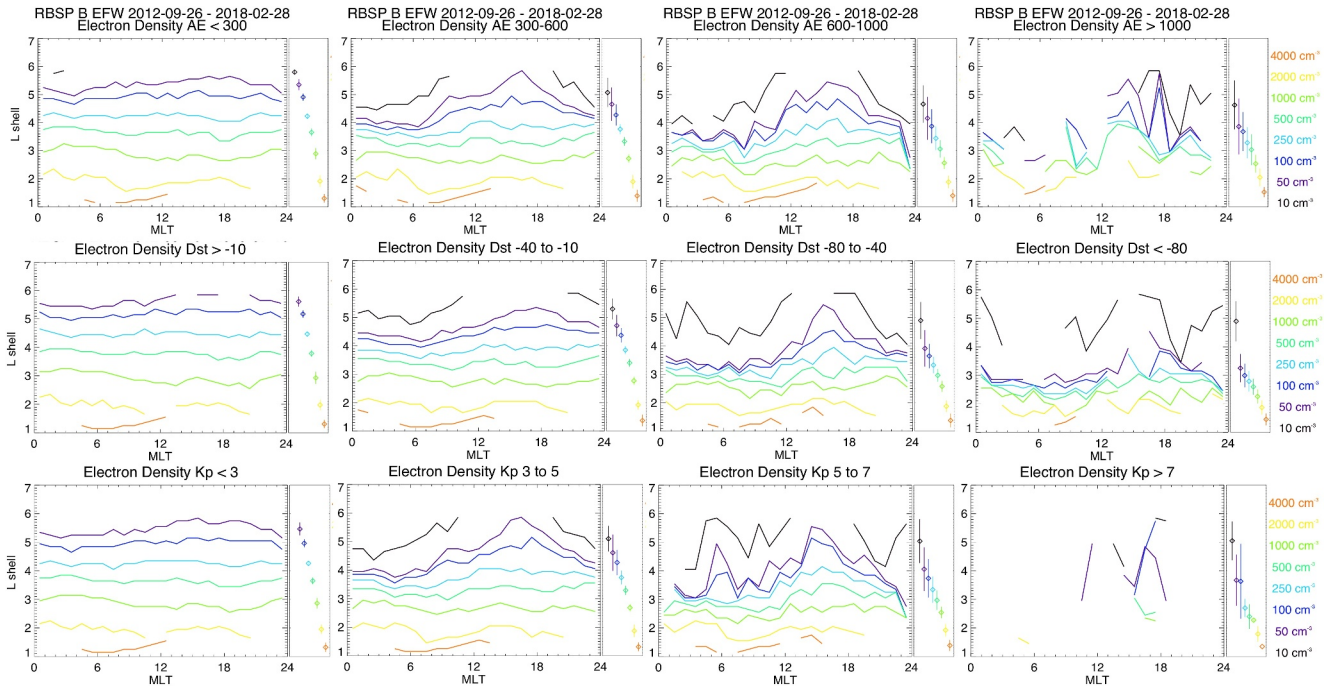

Figure 9. The s/c charging EFW sample mean electron plasma density with respect to L-shell and MLT from (red) 4,000 cm^{-3} down to (blue) 10 cm^{-3} for the 4 bins from low activity (left) to highest (right) of (top) Dst, (middle) Kp, (bottom) AE geomagnetic index bins. Each figure is composed of a side right box containing (diamond) the mean density located at a mean L-shell and (bars) the standard deviation of a given density level with respect to (MLT, L-shell).

and the mean density in each of bins. Most of density fits during quiet and moderate geomagnetic activity are made from L = 2 to L = 5.9 and have low error, below ∼10%. For high activity bins, density fits have larger fitting errors. To reduce the highest errors, we found the L-shell range had to be divided into two pieces, each with a dedicated fit, generally for active times. This introduces a L_{mid} in the L ∼ 3–4 region, that can be understood as playing the role of a statistical plasmapause separating two different regimes. Strictly speaking, L_{mid}, has not been chosen to satisfy any of the properties of the plasmapause previously described. However, it is made to best fit density profiles which do show discontinuities associated to the plasmapause formed by a density gradient. For instance, a density discontinuity occurs at L = 3 when Dst < −80 and MLT = [3,9], at L = 3.5 when −80 < Dst < −40 and MLT = [21,3], and also L = 3.5 when −80 < Dst < −40 and MLT = [3,9]. Otherwise, when a discontinuity in fit does not occur, threshold values, such as L_{100}, can be used to determine the plasmapause location. L_{100} would be fully compatible with the model in Ripoll et al. (2022) generated from the same database but readers could adjust the plasmapause location to be at the L_{50} or L_{30} density level given by the present modeling if they needed. A simple way to use both studies for quasi-linear computations is to use the present density fits to precompute local diffusion coefficients in (L, MLT, activity) for any given wave. A drift average may (or may not) be applied afterward according to the duration of the event to simulate or the MLT occurrence of the wave (or both). As the Fokker-Planck code is next ran for an event, it should call the $L_{100/pp}$ model of Ripoll et al. (2022) at each time step to separate in (L, MLT, activity) plasmaspheric waves from plasma trough waves and call accordingly the diffusion coefficients of either plasmaspheric waves or plasma trough waves for a given (L, MLT, activity).

3.5. MLT-Dependence of Specific Density Level Lines

Figure 9 shows some relevant mean level lines and their variation with MLT for the 4 bins of geomagnetic conditions. Mean L-shell, mean density, and standard deviations with respect to both (L, MLT) are also shown on the right panel of each figure with symbols and bars. Lines of mean levels below 500 cm^{-3} are much closer to each other on the night side than on the day side. The plasmapause is here well approximated by the 100 cm^{-3} level (see quantification of this approximation in Figures 2a and 2b of Ripoll et al. (2022)). The plasmapause is sharper on the night side and becomes a thick layer on the dayside. During quiet times and low activity (left column), the mean 10 cm^{-3} level expands beyond RBSP-B apogee leading to an

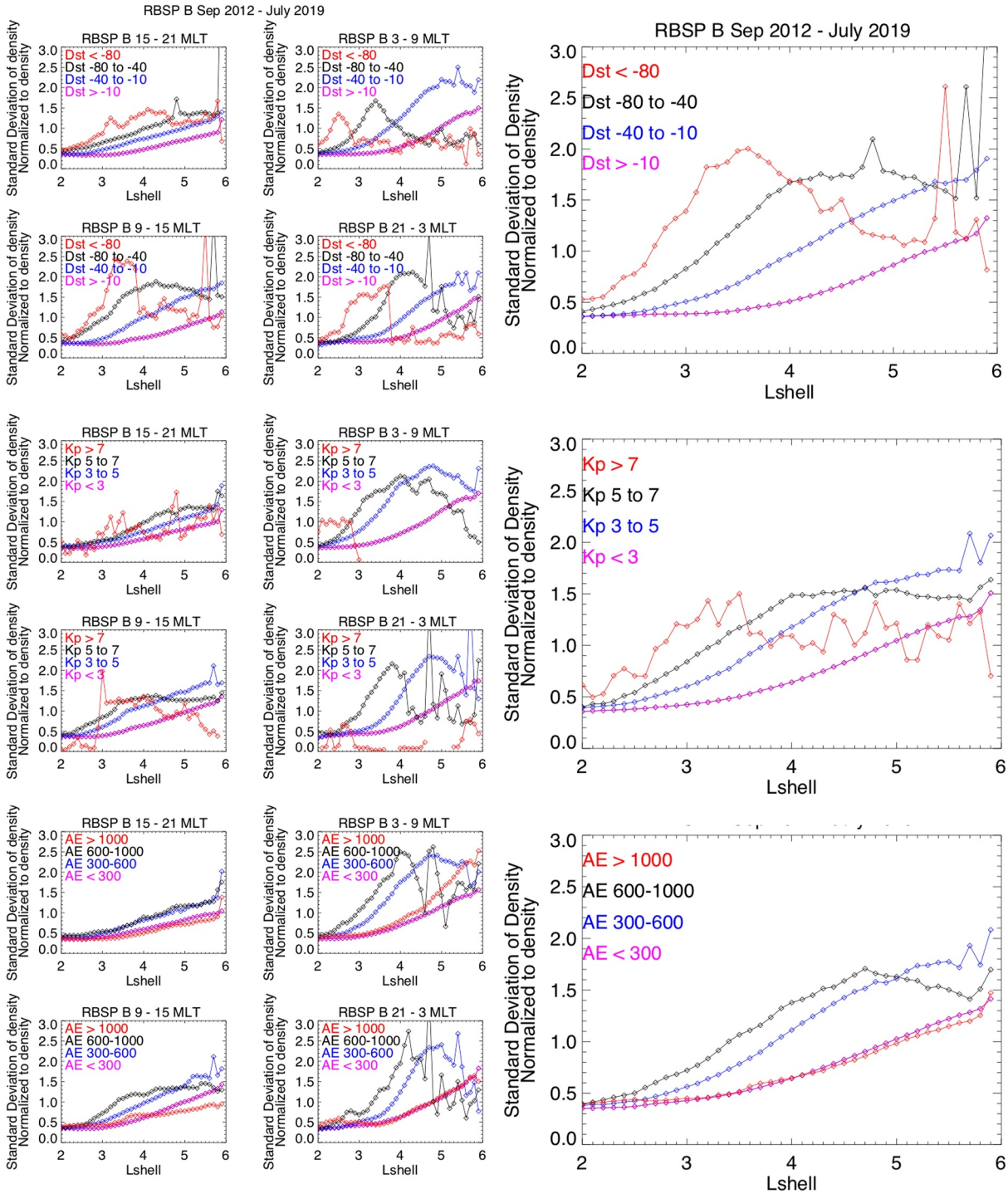

Figure 10. The standard deviation of the s/c charging RPSB-B/EFW electron plasma density normalized by the mean density measured at different MLT sectors (left column the day side, 9–21 MLT, and right column the night side, 21–3 MLT, clockwise in the order of dusk/dawn/noon/midnight) and sorted by (top) Dst, (center), Kp index, and (bottom) AE index for the whole RBSP-B mission. Fits of the density standard deviation line plots (in $\log_{10}$, without normalization by the mean density) are also provided in Tables 1–3.

undefined level line for some MLTs. Higher mean levels show little dispersion of ±0.2 L in MLT, with a flat shape. For moderate activity (second column), the asymmetry forms for mean levels below 500 cm^{-3} above L ~ 3.5 with the Kp and AE binning. Higher mean density levels remain symmetric (which is different for density binned with Dst). For active times (third column), the choice of the geomagnetic index (and its bin

width) directly affects the density mean profile and its variation with respect to MLT. For low activity, the density standard deviation is particularly small, well established, which enables an accurate prediction of the quiet time radiation belts.

3.6. Standard Deviation of the Electron Plasma Density

Figure 10 presents the density standard deviation normalized by the mean plasma density of the s/c charging EFW electron plasma density, $\Delta n_e/n_e$. The highest density standard deviation is a factor 3 of the mean density occurring when density is sorted by Dst and above L = 5. Large variations ($\Delta n_e/n_e \sim 2.5$) also occur at lower L-shell (L = 3–4) on the dayside during the most active Dst bin. These errors correspond to low density values in the plasma through. The direct response of the electron density to storm conditions corresponds to an increase of the density standard deviation, from a factor 2 to 3 of the mean density above L = 3.

When density is sorted with respect to Kp and AE, the MLT-average variations of $\Delta n_e/n_e$ are bounded by 2. For instance, for Kp in (5,7), the variation is flat with a value of ∼1.5 for L > 4. Largest variations on the night and dusk side can reach 2.5 or 3. During moderate activity (Kp = 3–5), the density standard variation can exceed twice the density between L = 4.5 and L = 5.5 on the dusk and night side. Variations associated with plume formation in the dusk sector for Kp in (5,7) represents $\Delta n_e/n_e \sim 1.3$ for L > 3.3 on the dayside up to 2 between L = 3 and 4.

The lowest standard deviation represents 0.35 to 0.5 of the density for quiet times below L = 4 and increases with L-shell up to ∼1.2 at L = 6, with density sorted by Kp or AE. These values slightly increase when sorted by Dst. This quantifies the constant evolution of the plasma density.

When density is sorted with AE, we do not find large variations at the lowest L-shells for the highest activity bin (AE > 1000) showing the influence of the storm, whether or not the statistics are averaged over MLT. Variations with increasing AE index are milder than for the Kp and Dst index. We do not see plume effects on the dayside either. We however do see some large variations with $\Delta n_e/n_e$ above 1.5 for L > 3.5 for the AE = 600–1,000 bin in both the dusk and night sector. This suggests sorting by AE mixes both density variations due to storm and substorms times. This interpretation is consistent with AE being a higher latitude index reported at higher cadence. A short duration burst of activity indicated by AE could inject energetic electrons into the inner magnetosphere giving rise to chorus, but not be of sufficient duration or spatial extent to significantly shape the plasmasphere. These results as well as those in Figure 8 may indicate that AE is not the most relevant parameter for density, which in turn complicates the problem as AE has been found relevant, for instance, to parametrize chorus waves (e.g., Li et al., 2009). That would signify waves and density cannot be parametrized with the same index and thus a single index cannot be used in radiation belt simulations.

Fits of the density standard deviation (without normalization by the mean density) are provided in Tables 1–3. Fits are defined as $\log_{10}(\Delta n_e(L)) = a_0 + a_1 L + a_2 L^2$, similarly to the choice made for fitting the mean density. The quantification of the fitting error is also provided. Plotting these fits (not shown) shows a smooth decaying density standard deviation with L-shell increasing, similarly to the density, explaining the low fitting errors as well as why we do not fit the more oscillating ratios of $\Delta n_e/n_e$ presented in Figure 10. This also confirms the increase of these ratios at large L-shell for active times is due to more fluctuating low density values of the plasma through. Further investigations of the shape of local density distributions are required in order to evaluate the applicability of the mean and standard deviations. This will be conducted in a future study.

4. Summary and Conclusions

In this article, we use the NASA Van Allen Probes mission data (2012–2019) in order to compute and provide new statistics of the electron density for L = 2 to L = 6. Three methods to deduce the electron density are presented, used, and compared, with the spacecraft charging method used widely to generate the final statistics and the upper hybrid frequency method used for verification.

New density statistics have been generated from EFW spacecraft charging using Probe B data from 12/2012 to 07/2019. The new statistics include various mean densities (Figures 8 and 9) and standard deviations (Figure 10) with respect to L-shell, magnetic local time (MLT), and geomagnetic conditions (for the AE, Kp, Dst geomagnetic

indices). New fitting laws are provided for both mean and standard deviation (Tables 1–3) for direct and easy use in radiation belt and space weather codes. These mean density laws are more evolved than former models from the literature due to their multiple dependences. The new mean values are generated to be directly applied in radiation belt physics and space weather codes, as the plasma density is one of the major parameters of the simulation of wave-particle interactions. Similarly, standard deviations can be used for uncertainty quantification and machine learning models. More investigation of the local density distributions is also needed to support the statistics and will be done in a next study.

We find no significant regular variations of the electron density with respect to magnetic latitude within ±20° of magnetic latitude, except at low L-shell. However, the electron density profile becomes oscillating in the plasmasphere-plasma trough region, with variations increasing with geomagnetic activity. At low L-shell, the latitudinal variation was obtained in Hartley et al. (2023) by combining Van Allen Probes data for latitude below 20° with Arase data above 20° up to 40° for $L \leq 3$.

For event-driven simulations of the radiation belts, we show how to build a global density model, which is defined for temporal bins of 4–9 hr at all L-shells. The model is made from the association of different sources of density measurements complemented with models when needed. This allows us to observe the evolution of the density over the years of the Van Allen Probes mission.

The evolution of the plasmasphere shows the f_{pe}/f_{ce0} ratio is generally below 10 for $L < 2.5$. Above $L = 3.5$, variability of this ratio is maximal, varying between ∼5 and ∼30, with highest ratios (more extended plasmasphere) more often seen during the strongest solar activity (years 2013 and 2014 with highest sunspot numbers). Plotted versus MLT, this ratio reveals a complex morphology for intermediate activity with high f_{pe}/f_{ce} forming a thick arc, starting near dawn, crossing the post-midnight sector, and merging into the dusk-side bulge region.

Differences between EFW and EMFISIS upper hybrid frequency mean densities (the reference density) have been quantified using Van Allen Probe A density measurements from 09/2012 to 04/2016. Although we note that the differences between EFW and EMFISIS mean densities can compensate in MLT due to the 8h sectors, the agreement is generally excellent, confirming the reliability of the statistics, in agreement with Jahn et al. (2020) and Ripoll et al. (2022). Differences are the largest at the highest L-shells for the lowest densities at which the s/c charging method can reach its lower density limit.

Converting the density difference into a L-shell difference, we find the difference committed on density represents often below 12% of the reference L-shell at which density was computed. For instance, a 10% variation of the 50 cm^{-3} level for Kp in (5,7) represents a ∼0.5 L difference at $L \sim 5$. Large differences of ∼1 L are found in the dawn sector during intense activity (Kp in (5,7)) at $L \sim 4$ within the plasmapause transition region ($n_e \sim 100$–200 cm^{-3}).

A hemispheric asymmetry of the plasma density below $L = 3$ is apparent in Figure 5 of Hartley et al. (2023). This may be dependent on season. Ripoll et al. (2021) showed that the smallest refractive index computed from lightning-generated whistlers were found during Northern hemisphere summer, which is consistent with what is referred to as the winter anomaly (a.k.a seasonal anomaly) for which the electron plasma density is abnormally greater in winter than in summer. Exploring these additional dependencies is planned as part of future analyses.

Main noticeable behaviors of the cold plasma electron density found in this study are sorted by activity and summarized in following:

Quiet times. The mean plasmasphere is azimuthally symmetric around Earth with respect to MLT for $Kp < 1$. The 100 cm^{-3} level can reach $L \sim 6$ during quiet activity. The mean 100 cm^{-3} level line is above $L = 5$ for $Kp < 1$. The mean 10 cm^{-3} level expands above RBSP-B apogee. Higher mean density levels show a small dispersion of ±0.2 L in MLT. For $Kp < 2$, mean 100 cm^{-3} level line is at $L = 5$ on the dayside and slightly below $L = 5$ on the nightside, indicative of a slight asymmetry forming. The lowest standard deviation represents a factor 0.5 of the density for quiet times below $L = 4$ and increases with L-shell up to a factor ∼1.2 at $L = 6$, with density sorted by Kp or AE (slightly higher if sorted by Dst). The electron outer belt lies within the plasmasphere for 60% of all times (i.e., all data).

Moderate activity times. As soon as activity increases ($Kp > 2$), we see the gradual MLT asymmetry increasing with higher mean density in the afternoon sector around ∼15–16 MLT due to plumes expanding outward. On the contrary, the mean density decreases on the dawn and night sectors. For $Kp = 3$–5, the density asymmetry forms

Table 1

Fits of Both the Mean Cold Plasma Density, $log_{10}(n_e(L)) = a_0 + a_1L + a_2L^2$ (in #/cm^3) and Its Standard Deviation (STD), $log_{10}(\Delta n_e(L)) = a_0 + a_1L + a_2L^2$ (in #/cm^3), Over a Given L-Shell Range Sorted by MLT Sectors and Dst Bins

			Mean density coeff.				Density STD coeff.				
MLT range		Index bin	0th	1st	2nd	Error	0th	1st	2nd	Error	L-range
15	21	Dst > −10	3.78	−0.21	−0.02	1.3	3.29	−0.27	0	5.8	2–5.9
15	21	−40 < Dst < −10	4.27	−0.47	0	3.3	3.42	−0.28	−0.01	4.5	2–5.9
15	21	−80 < Dst < −40	4.69	−0.70	0.02	11.4	4.07	−0.57	0.02	11.7	2–5.9
15	21	Dst < −80	5.58	−1.27	0.09	13.7	4.25	−0.64	0.02	20.2	2–5.9
15	21	Dst all	3.95	−0.31	−0.01	1.0	3.24	−0.21	−0.01	4.2	2–5.9
3	9	Dst > −10	3.41	0.08	−0.07	1.4	2.87	0.04	−0.04	6.3	2–5.9
3	9	−40 < Dst < −10	2.70	0.68	−0.20	2.1	2.87	0.11	−0.06	1.3	2–3.5
3	9	−40 < Dst < −10	10.25	−2.97	0.23	7.9	7.25	−1.73	0.12	8.3	3.5–5.9
3	9	−40 < Dst < −10	5.15	−0.82	0.01	25.9	4.08	−0.48	0	21.3	2–5.9
3	9	−80 < Dst < −40	−0.04	3.13	−0.75	4.3	−1.39	3.59	−0.75	10.7	2–3.5
3	9	−80 < Dst < −40	3.16	−0.82	0.08	15.7	0.48	0.23	−0.03	45.0	3.5–5.9
3	9	Dst < −80	7.97	−2.80	0.23	11.5	1.82	2.14	−0.76	19.8	2–3
3	9	Dst < −80	4.64	−1.44	0.15	22.3	2.46	−0.63	0.07	76.3	3–5.9
3	9	Dst all	3.77	−0.12	−0.05	3.7	2.78	0.13	−0.06	2.8	2–5.9
9	15	Dst > −10	3.38	0.03	−0.05	2.4	2.92	−0.04	−0.03	5.7	2–5.9
9	15	−40 < Dst < −10	4.07	−0.31	−0.03	6.7	2.83	0.08	−0.05	7.0	2–5.9
9	15	−80 < Dst < −40	5.38	−1.15	0.08	9.6	3.66	−0.32	−0.01	9.9	2–5.9
9	15	Dst < −80	9.54	−4.23	0.60	15.6	8.76	−4.17	0.68	13.8	2–3.5
9	15	Dst < −80	−2.38	1.79	−0.21	20.0	4.51	−0.94	0.06	39.3	3.5–5.9
9	15	Dst < −80	5.82	−1.57	0.13	25.4	5.03	−1.14	0.08	32.6	2–5.9
9	15	Dst all	3.62	−0.10	−0.04	1.9	2.76	0.09	−0.05	5.0	2–5.9
21	3	Dst > −10	3.36	0.11	−0.07	1.7	3.09	−0.06	−0.03	6.7	2–5.9
21	3	−40 < Dst < −10	3.88	−0.12	−0.07	12.1	2.74	0.21	−0.08	7.2	2–5.9
21	3	−80 < Dst < −40	2.34	1.11	−0.32	2.7	2.45	0.50	−0.14	3.7	2–3.5
21	3	−80 < Dst < −40	3.73	−0.84	0.06	19.0	11.13	−3.65	0.33	15.2	3.5–5.9
21	3	Dst < −80	5.03	−0.68	−0.08	12.9	1.69	1.34	−0.37	8.6	2–3.5
21	3	Dst < −80	0.85	0.25	−0.04	16.9	2.67	−0.75	0.08	40.4	3.5–5.9
21	3	Dst all	3.56	0.01	−0.06	2.2	2.80	0.12	−0.05	4.1	2–5.9
All		Dst > −10	3.48	−0.01	−0.05	0.9	3.07	−0.09	−0.02	3.8	2–5.9
All		−40 < Dst < −10	4.29	−0.42	−0.02	10.1	3.21	−0.10	−0.03	7.2	2–5.9
All		−80 < Dst < −40	5.67	−1.27	0.08	13.6	4.40	−0.72	0.04	15.7	2–5.9
All		Dst < −80	5.82	−1.53	0.12	11.6	4.31	−0.72	0.03	18.7	2–5.9
All		Dst all	3.74	−0.15	−0.04	2.1	2.93	0.01	−0.04	1.9	2–5.9

Note. a_0, a_1, and a_2 are, respectively, the 0th, 1st, and 2nd coefficients for (left) the mean and (right) the STD. The error of each fit, computed as the mean percent difference, is provided. The L-shell range over which the fit is made is adjusted by the interpolating subroutine according to the availability of the statistics. Some cases require the fits to be made on more than a single L-shell range. Both mean and STD are established on the same L-shell range. Binning with respect to the Kp and AE indices are given in Tables 2 and 3.

Table 2
Same as Table 1 for Kp Bins

MLT range		Index bin	Mean density coeff. 0th	1st	2nd	Error	Density STD coeff. 0th	1st	2nd	Error	L-range
15	21	Kp < 3	3.91	−0.29	−0.02	0.9	3.21	−0.20	−0.01	4.5	2–5.9
15	21	3 < Kp < 5	4.11	−0.38	−0.01	2.4	3.45	−0.28	0	3.7	2–5.9
15	21	5 < Kp < 7	4.62	−0.65	0.02	10.0	3.51	−0.28	−0.01	6.2	2–5.9
15	21	Kp > 7	5.87	−1.53	0.13	12.7	2.94	−0.06	−0.06	27.8	2–4
15	21	Kp > 7	8.35	−2.54	0.22	35.1	6.50	−1.97	0.18	49.1	4–5.9
15	21	Kp > 7	6.27	−1.78	0.16	24.0	6.10	−1.81	0.16	56.4	2–5.9
15	21	all Kp	3.95	−0.31	−0.01	1.0	3.24	−0.21	−0.01	4.2	2–5.9
3	9	Kp < 3	3.64	−0.04	−0.06	3.4	2.76	0.13	−0.05	4.3	2–5.9
3	9	3 < Kp < 5	2.39	1.01	−0.29	2.4	2.78	0.26	−0.11	2.1	2–3.5
3	9	3 < Kp < 5	7.40	−1.97	0.15	5.3	5.83	−1.20	0.07	4.9	3.5–5.9
3	9	5 < Kp < 7	5.46	−1.21	0.08	10.3	2.56	0.38	−0.12	10.4	2–5.9
3	9	Kp > 7	12.52	−6.46	0.96	20.9	−9.66	10.84	−2.36	34.0	2–3
3	9	all Kp	3.77	−0.12	−0.05	3.7	2.78	0.13	−0.06	2.8	2–5.9
9	15	Kp < 3	3.55	−0.06	−0.05	1.9	2.78	0.06	−0.04	5.7	2–5.9
9	15	3 < Kp < 5	4.10	−0.36	−0.02	3.4	2.82	0.10	−0.05	6.1	2–5.9
9	15	5 < Kp < 7	4.68	−0.76	0.04	5.0	3.41	−0.20	−0.02	6.4	2–5.9
9	15	Kp > 7	16.53	−9.66	1.60	30.1	−9.66	10.84	−2.36	34.0	2–3.5
9	15	Kp > 7	6.69	−1.85	0.16	27.8	7.94	−2.11	0.16	33.8	3.5–5.9
9	15	all Kp	3.62	−0.10	−0.04	1.9	2.76	0.09	−0.05	5.0	2–5.9
21	3	Kp < 3	3.44	0.07	−0.07	1.3	2.85	0.08	−0.05	5.4	2–5.9
21	3	3 < Kp < 5	3.47	0.07	−0.08	1.7	3	−0.01	−0.03	2.2	2–3.5
21	3	3 < Kp < 5	9.08	−2.45	0.18	7.2	4.57	−0.48	−0.02	11.9	3.5–5.9
21	3	5 < Kp < 7	1.89	1.55	−0.43	4.4	−0.28	2.63	−0.54	13.4	2–4
21	3	5 < Kp < 7	−0.55	0.72	−0.08	10.1	−0.55	0.67	−0.07	32	4–5.9
21	3	Kp > 7	11.46	−5.65	0.79	28.8	6.41	−2.65	0.25	56.4	2–4
21	3	Kp > 7	8.89	−3.28	0.34	31.8	5.58	−2.78	0.35	65.7	4–5.9
21	3	all Kp	3.56	0.01	−0.06	2.2	2.80	0.12	−0.05	4.1	2–5.9
15	21	Kp < 3	3.91	−0.29	−0.02	0.9	3.21	−0.20	−0.01	4.5	2–5.9
All		Kp < 3	3.65	−0.09	−0.05	1.7	2.93	0	−0.04	2.7	2–5.9
All		3 < Kp < 5	4.49	−0.56	0	8.3	3.29	−0.13	−0.03	6.8	2–5.9
All		5 < Kp < 7	5.07	−0.95	0.05	6.7	3.69	−0.34	−0.01	8.8	2–5.9
All		Kp > 7	5.69	−1.60	0.16	15.7	3.15	−0.04	−0.07	17.1	2–4
All		Kp > 7	−2.92	2.07	−0.24	26.9	−5.89	3.35	−0.37	34.9	4–5.9
All		Kp > 7	4.97	−1.16	0.09	24.6	2.87	−0.05	−0.05	32.6	2–5.9
All		all Kp	3.74	−0.15	−0.04	2.1	2.93	0.01	−0.04	1.9	2–5.9

Note. Fits of both the mean density and the density standard deviation over a given L-shell range sorted by MLT and Kp bins.

Table 3
Same as Table 2 for AE Bins

MLT range		Index bin	Mean density coeff. 0th	1st	2nd	Error	Density STD coeff. 0th	1st	2nd	Error	L-range
15	21	AE < 300	3.97	−0.30	−0.02	1.5	3.15	−0.15	−0.02	2.6	2–5.9
15	21	300 < AE < 600	4.22	−0.45	0	2.9	3.47	−0.30	0	5.4	2–5.9
15	21	600 < AE < 1000	4.33	−0.49	0	8.4	3.55	−0.30	−0.01	5.4	2–5.9
15	21	AE > 1000	4.35	−0.56	0.02	3.4	1.26	1.12	−0.21	6.8	2–3.5
15	21	AE > 1000	3.27	−0.23	−0.02	37	−2.37	2.19	−0.27	51.8	3.5–5.9
15	21	AE > 1000	4.49	−0.56	−0.01	32.8	2.79	0.10	−0.06	46.8	2–5.9
15	21	all AE	4.02	−0.34	−0.01	1.9	3.21	−0.17	−0.02	2.8	2–5.9
3	9	AE < 300	3.68	−0.06	−0.06	4.9	2.85	0.09	−0.05	1.2	2–5.9
3	9	300 < AE < 600	2.46	0.93	−0.26	1.5	1.93	0.83	−0.19	1.9	2–4
3	9	300 < AE < 600	8.99	−2.64	0.22	4.8	6.05	−1.29	0.08	7.1	4–5.9
3	9	600 < AE < 1000	2.91	0.69	−0.26	2.7	1.88	0.97	−0.24	3.5	2–3.5
3	9	600 < AE < 1000	11.59	−4.17	0.42	20.1	24.04	−9.18	0.91	72	3.5–5.9
3	9	AE > 1000	6.41	−2.01	0.23	13.7	−1.08	2.57	−0.43	21.0	2–4
3	9	AE > 1000	−2.67	1.64	−0.17	22.2	0.11	0.42	−0.05	60.3	4–5.9
3	9	all AE	3.85	−0.16	−0.04	5.6	2.87	0.09	−0.05	1.9	2–5.9
9	15	AE < 300	3.5	−0.03	−0.05	1.8	2.70	0.08	−0.04	6.5	2–5.9
9	15	300 < AE < 600	4.04	−0.33	−0.02	3.2	2.84	0.06	−0.04	4.2	2–5.9
9	15	600 < AE < 1000	4.49	−0.65	0.02	4.6	2.86	0.06	−0.05	3.9	2–5.9
9	15	AE > 1000	4.06	−0.49	0.01	15.5	2.82	0.07	−0.05	13.2	2–5.9
9	15	all AE	3.59	−0.08	−0.05	1.5	2.70	0.10	−0.05	5.2	2–5.9
21	3	AE < 300	3.37	0.14	−0.08	2.5	2.72	0.17	−0.06	2.4	2–5.9
21	3	300 < AE < 600	3.20	0.27	−0.12	1.9	2.70	0.16	−0.06	2.6	2–3.5
21	3	300 < AE < 600	14.55	−4.77	0.42	14.1	15.81	−5.15	0.45	71	3.5–5.9
21	3	600 < AE < 1000	3.78	−0.03	−0.09	6.8	2.72	0.25	−0.08	5.7	2–3.5
21	3	600 < AE < 1000	2.78	−0.77	0.08	34.4	6.39	−2.14	0.21	49.6	3.5–5.9
21	3	AE > 1000	0.24	2.9	−0.70	10.3	−0.68	3.10	−0.66	13.2	2–3.5
21	3	AE > 1000	1.68	−0.18	0.01	19.1	0.80	−0.01	0.01	69.5	3.5–5.9
21	3	all AE	3.53	0.05	−0.07	4.2	2.65	0.22	−0.07	2.4	2–5.9
All		AE < 300	3.64	−0.07	−0.05	2.8	2.88	0.04	−0.04	1.6	2–5.9
All		300 < AE < 600	4.53	−0.58	0	10.3	3.30	−0.15	−0.03	6.3	2–5.9
All		600 < AE < 1000	5.10	−0.95	0.05	9.8	3.61	−0.31	−0.01	7.6	2–5.9
All		AE > 1000	4.71	−0.79	0.05	3.4	1.81	0.91	−0.20	4.4	2–3.5
All		AE > 1000	5.71	−1.30	0.10	15.9	5.80	−1.27	0.09	13.4	3.5–5.9
All		AE > 1000	5.41	−1.16	0.08	16.0	4.01	−0.52	0.02	20.1	2–5.9
All		all AE	3.76	−0.15	−0.04	3.5	2.89	0.05	−0.05	1.8	2–5.9

Note. Fits of both the mean density and the density standard deviation over a given L-shell range sorted by MLT and AE bins.

for a mean density below the 500 cm^{-3} level above L ~ 3.5. The mean density is between ~500 cm^{-3} and ~50 cm^{-3} between L ~ 4 and L ~ 6 during quiet and moderately active times (Kp < 3), representing more than 80% of all times. We find the percent difference between the EFW and EMFISIS reference densities is bounded by ±20% for quiet and moderate activity (Kp < 5) when all MLTs are averaged together.

Intense activity times. The high mean density region below L = 2 is statistically undetermined both on the night and day sides. Differences between EFW and EMFISIS upper hybrid frequency mean densities can reach ±30%. The highest standard deviation is a factor 2.5 to 3 of the mean density, when density is sorted by Dst above L = 5. Sorting density with respect to Dst, we find a direct response of the mean electron density to storm conditions, with standard variations of the electron density ranging from a factor 2 to 3 above L = 3 for Dst < −80. There is a saturation effect of the mean density variations with the AE index for which the two highest activity bins show a similar L-shell position of the density levels, contrary to the Kp and Dst binning. This may indicate that AE is not the most relevant parameter for the plasmaspheric density for active conditions.

Extreme activity times. The high mean density region below L = 2 is now undetermined both on the night and day sides. Differences between EFW and EMFISIS mean densities can reach ±100%. Density variations represent a factor 2.5 to 3 of the mean density and occur above L = 5. Variations by a factor 2.5 also occur at lower L-shell (L = 3–4) on the day side. MLT-statistics are not adequate for extreme activity.

All times except extreme activity times. At L-shell below L = 2, the density on the night side is undetermined due to eclipse times for all geomagnetic conditions. Eclipse periods can also extend to higher L shell, such as when the spacecraft is in the equatorial plane. At low L-shell, the largest variations due to geomagnetic activity occur in the night sector. The densities derived from plasmaspheric waves (the third method presented in Section 2) are available more than 50% of the time for 1 < L < 2 and are used for complementing the present density database at low L-shell (see Hartley et al. (2023)). Further deduction of the plasma density from ground-based measurements of whistler data is also a promising method to complement this density database (e.g., Lichtenberger (2009)). Dusk is the least sensitive MLT sector to activity, with a variation by ±0.25 L for the 500 cm^{-3} mean density level for all Kp < 7. This may be explained by the large density values due to plasmaspheric expansion during moderately to active times.

The plasmapause as approximated by the 100 cm^{-3} level is sharper on the night side and becomes a thick layer on the dayside. The plasmapause and its statistics are generated both from the gradient method (e.g., Carpenter and Anderson (1992); O'Brien and Moldwin (2003)) and the 100 cm^{-3} density lines and discussed in detail in a companion article dedicated to the statistics and empirical modeling of the plasmapause position (Ripoll et al., 2022). The 100 cm^{-3} density lines, L_{100}, serving as a plasmapause marker, of our study is fully compatible with the one of Ripoll et al. (2022) as they are both extracted from the EFW s/c density database of the present study.

The results suggest that the AE index is not the most relevant parameter for parametrizing the density, which in turn complicates radiation belt modeling as AE has been found relevant for the parametrization of chorus waves. That would signify waves and density cannot be parametrized with the same index and thus a single index cannot be used in radiation belt simulations.

Data Availability Statement

Van Allen Probes A EMFISIS data are available at https://doi.org/10.48322/c4ha-xj50. Van Allen Probes B EMFISIS data are available at https://doi.org/10.48322/c6s1-wg66. Van Allen Probes wave data used in this work are also available from the EFW and EMFISIS team websites (which one can find at http://rbspgway.jhuapl.edu).

Acknowledgments
The authors thank the EFW and EMFISIS teams of the Van Allen Probes mission for their support. The work of J-FR and GC was performed under the auspices of an agreement between CEA/DAM (Commissariat à l'Energie Atomique, Direction des Applications Militaries) and NNSA/DP (National Nuclear Security Administration, Defense Program) on cooperation on fundamental science. J-FR thank the Direction Générale de l'Armement (DGA) and the Agence pour l'Innovation de Défense (AID) for funding the ASTRID project "PACTE-ESPACE." Part of the research of J-FR, DM, VP and GC was supported by the International Space Science Institute (ISSI) in Bern, through ISSI International Team project #477 (Radiation Belt Physics From Top To Bottom: Combining Multipoint Satellite Observations And Data Assimilative Models To Determine The Interplay Between Sources And Losses). The authors thank the National Science Foundation Geospace Environment Modeling Project 2040708. D.P.H. acknowledges NASA Grants 80NSSC20K1324 and 80NSSC21K0519. D.P.H. and G.S.C. acknowledge NSF-GEM Grant 2040708. V.P. acknowledges the project 21GRD02 BIOSPHERE (www.euramet-biosphere.eu) from the European Partnership on Metrology, co-financed by the European Union's Horizon Europe Research and Innovation Programme and by the participating states, and the project PITHIA-NRF (https://www.pithia-nrf.eu/) INFRAIA-02-2020, ID 101007599 (Plasmasphere Ionosphere Thermosphere Integrated Research Environment and Access services: a Network of Research Facilities). Funded under NASA HGIO 80NSSC21K0584, NASA HGIO 80NSSC21K0519, and NSF-GEM Grant 2040708, 21GRD02 BIOSPHERE, INFRAIA-02-2020, ID 101007599, and ANR ASTRID PACTE-ESPACE.

References

Anderson, P. C., Carpenter, D. L., Tsuruda, K., Mukai, T., & Rich, F. J. (2001). Multisatellite observations of rapid subauroral ion drifts (SAID). *Journal of Geophysical Research*, *106*(A12), 29585–29599. https://doi.org/10.1029/2001JA000128

Borovsky, J. E., & Denton, M. H. (2008). A statistical look at plasmaspheric drainage plumes. *Journal of Geophysical Research*, *113*(A9), A09221. https://doi.org/10.1029/2007JA012994

Borovsky, J. E., Friedel, R. H. W., & Denton, M. H. (2014). Statistically measuring the amount of pitch angle scattering that energetic electrons undergo as they drift across the plasmaspheric drainage plume at geosynchronous orbit. *Journal of Geophysical Research: Space Physics*, *119*(3), 1814–1826. https://doi.org/10.1002/2013JA019310

Breneman, A. W., Wygant, J. R., Tian, S., Cattell, C. A., Thaller, S. A., Goetz, K., et al. (2022). The Van Allen Probes electric field and waves instrument: Science results, measurements, and access to data. *Space Science Reviews*, *218*(8), 69. https://doi.org/10.1007/s11214-022-00934-y

J. Burch, M. Schulz, & H. Spence (2005). *Inner magnetosphere interactions: New perspectives from imaging* (Vol. 159). *Geophysical Monograph*. Published by the American Geophysical Union. https://doi.org/10.1029/159GM02

Carpenter, D. L. (1963). Whistler evidence of a 'knee' in the magnetospheric ionization density profile. *Journal of Geophysical Research*, *68*(6), 1675–1682. https://doi.org/10.1029/jz068i006p01675

Carpenter, D. L. (1966). Whistler studies of the plasmapause in the magnetosphere. 1. Temporal variations in the position of the knee and some evidence on plasma motions near the knee. *Journal of Geophysical Research*, *71*(3), 693–709. https://doi.org/10.1029/jz071i003p00693

Carpenter, D. L. (1970). Whistler evidence of the dynamic behavior of the duskside bulge in the plasmasphere. *Journal of Geophysical Research*, *75*(19), 3837–3847. https://doi.org/10.1029/ja075i019p03837

Carpenter, D. L., & Anderson, R. R. (1992). An ISEE/whistler model of equatorial electron density 740 in the magnetosphere. *Journal of Geophysical Research*, *97*(A2), 1097–1108. https://doi.org/10.1029/91JA01548

Carpenter, D. L., Giles, B. L., Chappell, C. R., Decreau, P. M. E., Anderson, R. R., Persoon, A. M., et al. (1993). Plasmasphere dynamics in the dusk-side bulge region: A new look at an old topic. *Journal of Geophysical Research*, *98*(A11), 19243–19271. https://doi.org/10.1029/93ja00922

Carpenter, D. L., & Lemaire, J. (1997). Erosion and recovery of the plasmasphere in the plasmapause region. *Space Science Reviews*, *80*, 153–179. https://doi.org/10.1007/978-94-009-0045-5_7

Carpenter, D. L., & Lemaire, J. (2004). The plasmasphere boundary layer. *Annales Geophysicae*, *22*(12), 4291–4298. https://doi.org/10.5194/angeo-22-4291-2004

Carpenter, D. L., & Smith, R. L. (1964). Whistler measurements of electron density in the 738 magnetosphere. *Reviews of Geophysics and Space Physics*, *2*(3), 415–441. https://doi.org/10.1029/91JA01548

Chappell, C. R. (1974). Detached plasma regions in the magnetosphere. *Journal of Geophysical Research*, *79*(13), 1861–1870. https://doi.org/10.1029/ja079i013p01861

Chappell, C. R., Harris, K. K., & Sharp, G. W. (1970). A study of the influence of magnetic activity on the location of the plasmapause as measured by OGO 5. *Journal of Geophysical Research*, *75*(1), 50–56. https://doi.org/10.1029/ja075i001p00050

Chu, X., Bortnik, J., Li, W., Ma, Q., Denton, R., Yue, C., et al. (2017). A neural network model of three-dimensional dynamic electron density in the inner magnetosphere. *Journal of Geophysical Research: Space Physics*, *122*(9), 9183–9197. https://doi.org/10.1002/2017JA024464

Dahmen, N., Sicard, A., Brunet, A., Santolik, O., Pierrard, V., Botek, E., et al. (2022). FARWEST: Efficient computation of wave-particle interactions for a dynamic description of the electron radiation belt diffusion. *Journal of Geophysical Research: Space Physics*, *127*(10), e2022JA030518. https://doi.org/10.1029/2022JA030518

Darrouzet, F., Décréau, P. M. E., De Keyser, J., Masson, A., Gallagher, D. L., Santolík, O., et al. (2004). Density structures inside the plasmasphere: Cluster observations. *Annals of Geophysics*, *22*(7), 2577–2585. https://doi.org/10.5194/angeo-22-2577-2004

Darrouzet, F., & De Keyser, J. (2013). The dynamics of the plasmasphere: Recent results. *Journal of Atmospheric and Solar-Terrestrial Physics*, *99*(2013), 53–60. https://doi.org/10.1016/j.jastp.2012.07.004

Darrouzet, F., De Keyser, J., & Pierrard, V. (Eds.) (2009a). *The Earth's plasmasphere: Cluster and IMAGE – A modern perspective* (p. 296). Springer.

Darrouzet, F., Gallagher, D. L., André, N., Carpenter, D. L., Dandouras, I., Décréau, P. M. E., et al. (2009b). Plasmaspheric density structures and dynamics: Properties observed by the CLUSTER and IMAGE missions. *Space Science Reviews*, *145*(1–2), 55–106. https://doi.org/10.1007/s11214-008-9438-9

Décréau, P. M. E., Fergeau, P., Krasnoselskikh, V., Le Guirriec, E., Levéque, M., Martin, P., et al. (2001). Whisper experimenters: Early results from the whisper instrument on Cluster: An overview. *Annals of Geophysics*, *19*(10/12), 1241–1258. https://doi.org/10.5194/angeo-19-1241-2001

Delzanno, G. L., Borovsky, J. E., Henderson, M. G., Resendiz Lira, P. A., Roytershteyn, V., & Welling, D. T. (2021). The impact of cold electrons and cold ions in magnetospheric physics. *Journal of Atmospheric and Solar-Terrestrial Physics*, *220*, 105599. https://doi.org/10.1016/j.jastp.2021.105599

Denton, R. E., Menietti, J. D., Goldstein, J., Young, S. L., & Anderson, R. R. (2004). Electron density in the magnetosphere. *Journal of Geophysical Research*, *109*(A9), A09215. https://doi.org/10.1029/2003JA010245

Denton, R. E., Takahashi, K., Galkin, I. A., Nsumei, P. A., Huang, X., Reinisch, B. W., et al. (2006). Distribution of density along magnetospheric field lines. *Journal of Geophysical Research*, *111*(A4), A04213. https://doi.org/10.1029/2005JA011414

Denton, R. E., Wang, Y., Webb, P. A., Tengdin, P. M., Goldstein, J., Redfern, J. A., & Reinisch, B. W. (2012). Magnetospheric electron density longterm (>1 day) refilling rates inferred from passive radio emissions measured by IMAGE RPI during geomagnetically quiet times. *Journal of Geophysical Research*, *2012*(A3), 117. https://doi.org/10.1029/2011ja017274

Dungey, J. W. (1961). Interplanetary magnetic field and the auroral zones. *Physical Review Letters*, *6*(2), 47–48. https://doi.org/10.1103/physrevlett.6.47

Escoubet, C. P., Pedersen, A., Schmidt, R., & Lindqvist, P. A. (1997). Density in the magnetosphere inferred from ISEE 1 spacecraft potential. *Journal of Geophysical Research*, *102*(A8), 17595–17609. https://doi.org/10.1029/97JA00290

Gallagher, D. L., Craven, P. D., & Comfort, R. H. (2000). Global core plasma model. *Journal of Geophysical Research*, *105*(A8), 18819–18833. https://doi.org/10.1029/1999JA000241

Glauert, S. A., & Horne, R. B. (2005). Calculation of pitch angle and energy diffusion coefficients with the PADIE code. *Journal of Geophysical Research*, *110*(A4), A04206. https://doi.org/10.1029/2004JA010851

Goldstein, J. (2006). Plasmasphere response: Tutorial and review of recent imaging results. *Space Science Reviews*, *124*(1–4), 203–216. https://doi.org/10.1007/s11214-006-9105-y

Goldstein, J., De Pascuale, S., Kletzing, C., Kurth, W., Genestreti, K. J., Skoug, R. M., et al. (2014a). Simulation of Van Allen Probes plasmapause encounters. *Journal of Geophysical Research: Space Physics*, *119*(9), 7464–7484. https://doi.org/10.1002/2014JA020252

Goldstein, J., Gallagher, D. L., Sandel, B. R., Davis, M., Molyneux, P., Veach, T., et al. (2022). Chapter 6 - The future of plasmaspheric extreme ultraviolet (EUV) imaging. In *Understanding the space environment through global measurements* (pp. 231–286). Elsevier. https://doi.org/10.1016/B978-0-12-820630-0.00010-6

Goldstein, J., Sandel, B. R., Forrester, W. T., & Reiff, P. H. (2003a). IMF- driven plasmasphere erosion of 10 July 2000. *Geophysical Research Letters*, *30*(3), 1146. https://doi.org/10.1029/2002GL016478

Goldstein, J., Sandel, B. R., Forrester, W. T., Thomsen, M. F., & Hairston, M. R. (2005). Global plasmasphere evolution 22–23 April 2001. *Journal of Geophysical Research*, *110*(A12), A12218. https://doi.org/10.1029/2005JA011282

Goldstein, J., Sandel, B. R., Reiff, P. H., & Hairston, M. R. (2003b). Control of plasmaspheric dynamics by both convection and sub-auroral polarization stream. *Geophysical Research Letters*, *30*(24), 2243. https://doi.org/10.1029/2003GL018390

Goldstein, J., Thomsen, M. F., & DeJong, A. (2014b). In situ signatures of residual plasmaspheric plumes: Observations and simulation. *J. Geophys. Res.Space Physics*, *119*(6), 4706–4722. https://doi.org/10.1002/2014JA019953

Goldstein, J., Usanova, M., Toledo-Redondo, S., Pierrard, V., Malaspina, D., Maruyama, N., et al. (2023). Geospace core plasma supply and refilling (CPSR): Science and observations for the next decade, decadal survey website. *Heliophysics 2024 Decadal Whitepapers*, *55*(3). https://doi.org/10.3847/25c2cfeb.d02a145a

Gringauz, K. I., Bezrukikh, V. V., Ozerov, V. D., & Rybchinskii, R. E. (1960). Investigation of interplanetary ionized gas, high energy electrons and solar corpuscular radiation by means of three-electrode traps for charge-carrying particles installed on the Second Soviet Space rocket. *Doklady Akademii Nauk SSSR*, *131*(6), 1301–1304.

Gringauz, K. I., Bezrukikh, V. V., Ozerov, V. D., & Rybchinskii, R. E. (1962). The study of interplanetary ionized gas, energetic electrons, and corpuscular radiation of the sun employing three-electrode charged particles traps on the second soviet space rocket. *Planetary and Space Science*, *9*(3), 103–107. (translation of Gringauz et al., 1960). https://doi.org/10.1016/0032-0633(62)90180-0

Hartley, D. P., Cunningham, G. S., Ripoll, J.-F., Malaspina, D. M., Kasahara, Y., Miyoshi, Y., et al. (2023). Using Van Allen Probes and Arase observations to develop an empirical plasma density model in the inner zone. *Journal of Geophysical Research: Space Physics*, *128*(3), e2022JA031012. https://doi.org/10.1029/2022JA031012

Hartley, D. P., Kletzing, C. A., De Pascuale, S., Kurth, W. S., & Santolík, O. (2018b). Determining plasmaspheric densities from observations of plasmaspheric hiss. *Journal of Geophysical Research: Space Physics*, *123*(8), 6679–6691. https://doi.org/10.1029/2018JA025658

Hartley, D. P., Kletzing, C. A., Santolík, O., Chen, L., & Horne, R. B. (2018a). Statistical properties of plasmaspheric hiss from Van Allen Probes observations. *Journal of Geophysical Research: Space Physics*, *123*(4), 2605–2619. https://doi.org/10.1002/2017JA024593

Hwang, J., & Yoon, P. H. (2018). High-frequency thermal fluctuations and instabilities in the radiation belt environment. *Journal of Geophysical Research: Space Physics*, *123*(11), 9239–9251. https://doi.org/10.1029/2018JA025643

Imhof, W. L., Voss, H. D., Walt, M., Gaines, E. E., Mobilia, J., Datlowe, D. W., & Reagan, J. B. (1986). Slot region electron precipitation by lightning, VLF chorus, and plasmaspheric hiss. *Journal of Geophysical Research*, *91*(A8), 8883–8894. https://doi.org/10.1029/ja091ia08p08883

Jahn, J., Goldstein, J., Kurth, W., Thaller, S., De Pascuale, S., Wygant, J., et al. (2020). Determining plasmaspheric density from the upper hybrid resonance and from spacecraft potential: How do they compare? *Journal of Geophysical Research: Space Physics*, *125*(3), 1–17. https://doi.org/10.1029/2019ja026860

Kletzing, C. A., Kurth, W. S., Acuna, M., MacDowall, R. J., Torbert, R. B., Averkamp, T., et al. (2013). The electric and magnetic field instrument suite and integrated science (EMFISIS) on RBSP. *Space Science Reviews*, *179*(1–4), 127–181. https://doi.org/10.1007/s11214-013-9993-6

Kotova, G., Verigin, M., & Bezrukikh, V. (2014). The effect of the Earth's optical shadow on thermal plasma measurements in the plasmasphere. *Journal of Atmospheric and Solar-Terrestrial Physics*, *120*, 9–14. https://doi.org/10.1016/j.jastp.2014.08.013

Kotova, G., Verigin, M., Lemaire, J., Pierrard, V., Bezrukikh, V., & Smilauer, J. (2018). Experimental study of the plasmasphere boundary layer using MAGION 5 data. *Journal of Geophysical Research: Space Physics*, *123*(2), 1251–1259. https://doi.org/10.1002/2017JA024590

Kotova, G. A. (2007). The Earth's plasmasphere: State of studies (A review). *Geomagnetism and Aeronomy*, *47*(4), 409–422. https://doi.org/10.1134/s0016793207040019

Kotova, G. A., & Bezrukikh, V. V. (2022). The density and temperature distributions of thermal protons in the magnetic equatorial plane of the Earth's plasmasphere according to the INTERBALL-1 spacecraft data. *Geomagnetism and Aeronomy*, *62*(5), 546–554. https://doi.org/10.1134/S0016793222050061

Kotova, G. A., Bezrukikha, V. V., Chugunina, D. V., Mogilevskya, M. M., & Chernyshov, A. A. (2023). Regular density inhomogeneities in the boundary layer of the plasmasphere. *Geomagnetism and Aeronomy*, *63*(6), 701–709. https://doi.org/10.1134/s0016793223600674

Kougblénou, S., Lointier, G., Décréau, P. M. E., Trotignon, J.-G., Rauch, J.-L., Vallières, X., et al. (2011). Lower hybrid resonances stimulated by the four CLUSTER relaxation sounders deep inside the plasmasphere: Observations and inferred plasma characteristics. *Annals of Geophysics*, *29*(11), 2003–2018. https://doi.org/10.5194/angeo-29-2003-2011

Kurth, W. S., De Pascuale, S., Faden, J. B., Kletzing, C. A., Hospodarsky, G. B., Thaller, S., & Wygant, J. R. (2015). Electron densities inferred from plasma wave spectra obtained by the Waves instrument on Van Allen Probes. *Journal of Geophysical Research: Space Physics*, *120*(2), 904–914. https://doi.org/10.1002/2014JA020857

LeDocq, M. J., Gurnett, D. A., & Anderson, R. R. (1994). Electron number density fluctuations near the plasmapause observed by the CRRES Spacecraft. *Journal of Geophysical Research*, *99*(A12), 23661–23671. https://doi.org/10.1029/94ja02294

Lejosne, S., & Mozer, F. S. (2017). Subauroral Polarization Streams (SAPS) duration as determined from Van Allen probe successive electric drift measurements. *Geophysical Research Letters*, *44*(18), 9134–9141. https://doi.org/10.1002/2017GL074985

Lemaire, J. F., & Gringauz, K. I. (1998). *The Earth's plasmasphere*. Cambridge University Press.

Li, W., Ni, B., Thorne, R. M., Bortnik, J., Nishimura, Y., Green, J. C., et al. (2014). Quantifying hiss-driven energetic electron precipitation: A detailed conjunction event analysis. *Geophysical Research Letters*, *41*(4), 1085–1092. https://doi.org/10.1002/2013GL059132

Li, W., Thorne, R. M., Angelopoulos, V., Bortnik, J., Cully, C. M., Ni, B., et al. (2009). Global distribution of whistler-mode chorus waves observed on the THEMIS spacecraft. *Geophysical Research Letters*, *36*(9), L09104. https://doi.org/10.1029/2009GL037595

Lichtenberger, J. (2009). A new whistler inversion method. *Journal of Geophysical Research*, *114*(A7), A07222. https://doi.org/10.1029/2008JA013799

Lointier, G., Darrouzet, F., Décréau, P. M. E., Vallières, X., Kougblénou, S., Trotignon, J. G., & Rauch, J.-L. (2013). Refilling process in the plasmasphere: A 3-D statistical characterization based on Cluster density observations. *Annals of Geophysics*, *31*(2), 217–237. https://doi.org/10.5194/angeo-31-217-2013

Malaspina, D., Ergun, R., Goldstein, J., Spittler, C., Andersson, L., Borovsky, J., et al. (2022). Plasma Imaging, LOcal Measurement, and Tomographic Experiment (PILOT): A mission concept for transformational multi-scale observations of mass and energy flow dynamics in Earth's magnetosphere. *Frontiers in Astronomy and Space Sciences*, *9*, 910730. https://doi.org/10.3389/fspas.2022.910730

Malaspina, D. M., Jaynes, A. N., Boulé, C., Bortnik, J., Thaller, S. A., Ergun, R. E., et al. (2016). The distribution of plasmaspheric hiss wave power with respect to plasmapause location. *Geophysical Research Letters*, *43*(15), 7878–7886. https://doi.org/10.1002/2016GL069982

Malaspina, D. M., Ripoll, J.-F., Chu, X., Hospodarsky, G., & Wygant, J. (2018). Variation in plasmaspheric hiss wave power with plasma density. *Geophysical Research Letters*, *45*(18), 9417–9426. https://doi.org/10.1029/2018GL078564

Mauk, B. H., Fox, N. J., Kanekal, S. G., Kessel, R. L., Sibeck, D. G., & Ukhorskiy, A. (2013). Science objectives and rationale for the radiation belt storm probes mission. *Space Science Reviews*, *179*(1–4), 3–27. https://doi.org/10.1007/s11214-012-9908-y

Meredith, N. P., Horne, R. B., Glauert, S. A., Thorne, R. M., Summers, D., Albert, J. M., & Anderson, R. R. (2006). Energetic outer zone electron loss timescales during low geomagnetic activity. *Journal of Geophysical Research*, *111*(A5), A05212. https://doi.org/10.1029/2005JA011516

Meredith, N. P., Horne, R. B., Sicard-Piet, A., Boscher, D., Yearby, K. H., Li, W., & Thorne, R. M. (2012). Global model of lower band and upper band chorus from multiple satellite observations. *Journal of Geophysical Research*, *117*(A10), A10225. https://doi.org/10.1029/2012JA017978

Millan, R. M., Ripoll, J.-F., Santolík, O., & Kurth, W. S. (2021). Early-time non-equilibrium pitch angle diffusion of electrons by whistler-mode hiss in a plasmaspheric plume associated with BARREL precipitation. *Frontiers in Astronomy and Space Science*, *8*, 776992. https://doi.org/10.3389/fspas.2021.776992

Miyoshi, Y., Shinohara, I., Takashima, T., Asamura, K., Higashio, N., Mitani, T., et al. (2018). Geospace exploration project ERG. *Earth Planets and Space*, *70*(1), 101. https://doi.org/10.1186/s40623-018-0862-0

Moldwin, M. B., Downward, L., Rassoul, H. K., Amin, R., & Anderson, R. R. (2002). A new model of the location of the plasmapause: CRRES results. *Journal of Geophysical Research*, *107*(A11), 1339. https://doi.org/10.1029/2001JA009211

Moldwin, M. B., Thomsen, M. F., Bame, S. J., McComas, D., & Reeves, G. D. (1995). The fine-scale structure of the outer plasmasphere. *Journal of Geophysical Research*, *100*(A5), 8021–8029. https://doi.org/10.1029/94JA03342

Mozer, F. S. (2016). DC and low-frequency double probe electric field measurements in space. *Journal of Geophysical Research: Space Physics*, *121*(11), 10942–10953. https://doi.org/10.1002/2016JA022952

Nishida, A. (1966). Formation of plasmapause, or magnetospheric plasma knee, by the combined action of magnetospheric convection and plasma escape from the tail. *Journal of Geophysical Research*, *71*(23), 5669–5679. https://doi.org/10.1029/jz071i023p05669

O'Brien, T. P., & Moldwin, M. B. (2003). Empirical plasmapause models from magnetic indices. *Geophysical Research Letters*, *30*(4), 1152. https://doi.org/10.1029/2002GL016007

Ozhogin, P., Tu, J., Song, P., & Reinisch, B. W. (2012). Field-aligned distribution of the plasmaspheric electron density: An empirical model derived from the IMAGE RPI measurements. *Journal of Geophysical Research*, *117*(A6), A06225. https://doi.org/10.1029/2011JA017330

Pedersen, A., Cattell, C. A., Falthammar, C.-G., Formisano, V., Linqvist, P. A., Mozer, F., & Torbert, R. (1984). Quasistatic electric field measurements with spherical double probes on the GEOS and ISEE satellites. *Space Science Reviews*, *37*(1984), 269. https://doi.org/10.1007/bf00226365

Pierrard, V., Botek, E., & Darrouzet, F. (2021a). Improving predictions of the 3D dynamic model of the plasmasphere. *Frontiers in Astronomy and Space Sciences*, *8*, 69. https://doi.org/10.3389/fspas.2021.681401

Pierrard, V., Botek, E., Ripoll, J.-F., Thaller, S. A., Moldwin, M. B., Ruohoniemi, M., & Reeves, G. (2021b). Links of the plasmapause with other boundary layers of the magnetosphere: Ionospheric convection, radiation belts boundaries, auroral oval. *Frontiers in Astronomy and Space Sciences*, *8*. https://doi.org/10.3389/fspas.2021.728531

Pierrard, V., & Cabrera, J. (2005). Comparisons between EUV/IMAGE observations and numerical simulations of the plasmapause formation. *Annales Geophysicae*, *23*(7), 2635–2646. https://doi.org/10.5194/angeo-23-2635-2005

Pierrard, V., Ripoll, J.-F., Cunningham, G., Botek, E., Santolik, O., Thaller, S., et al. (2021c). Observations and simulations of dropout events and flux enhancements in October 2013: Comparing MEO equatorial with LEO polar orbit. *Journal of Geophysical Research: Space Physics*, *126*(6), e2020JA028850. https://doi.org/10.1029/2020JA028850

Reidy, J. A., Horne, R. B., Glauert, S. A., Clilverd, M. A., Meredith, N. P., Woodfield, E. E., et al. (2021). Comparing electron precipitation fluxes calculated from pitch angle diffusion coefficients to LEO satellite observations. *Journal of Geophysical Research: Space Physics*, *126*(3), e2020JA028410. https://doi.org/10.1029/2020JA028410

Reinisch, B. W., Huang, X., Song, P., Green, J. L., Fung, S. F., Vasyliunas, V. M., et al. (2004). Plasmaspheric mass loss and refilling as a result of a magnetic storm. *Journal of Geophysical Research*, *109*(A1), A01202. https://doi.org/10.1029/2003JA009948

Ripoll, J.-F., Claudepierre, S. G., Ukhorskiy, A. Y., Colpitts, C., Li, X., Fennell, J., & Crabtree, C. (2020a). Particle dynamics in the Earth's radiation belts: Review of current research and open questions. *Journal of Geophysical Research: Space Physics*, *125*(5), e2019JA026735. https://doi.org/10.1029/2019JA026735

Ripoll, J.-F., Denton, M., Loridan, V., Santolík, O., Malaspina, D., Hartley, D. P., et al. (2020c). How whistler mode hiss waves and the plasmasphere drive the quiet decay of radiation belts electrons following a geomagnetic storm. *Journal of Physics: Conference Series*, *1623*, 012005. https://doi.org/10.1088/1742-6596/1623/1/012005

Ripoll, J.-F., Denton, M. H., Hartley, D. P., Reeves, G. D., Malaspina, D., Cunningham, G. S., et al. (2020b). Scattering by whistler-mode waves during a quiet period perturbed by substorm activity. *Journal of Atmospheric and Solar-Terrestrial Physics*, *215*, 105471. https://doi.org/10.1016/j.jastp.2020.105471

Ripoll, J.-F., Farges, T., Malaspina, D. M., Cunningham, G. S., Hospodarsky, G. B., Kletzing, C. A., & Wygant, J. R. (2021). Propagation and dispersion of lightning-generated whistlers measured from the Van Allen Probes. *Frontiers in Physiology*, *9*, 722355. https://doi.org/10.3389/fphy.2021.722355

Ripoll, J.-F., Loridan, V., Denton, M. H., Cunningham, G., Reeves, G., Santolík, O., et al. (2019). Observations and Fokker-Planck simulations of the L-shell, energy, and pitch angle structure of Earth's electron radiation belts during quiet times. *Journal of Geophysical Research: Space Physics*, *124*(2), 1125–1142. https://doi.org/10.1029/2018ja026111

Ripoll, J.-F., Pierrard, V., Cunningham, G. S., Chu, X., Sorathia, K., Hartley, D., et al. (2023). Modeling of the cold electron plasma density for radiation belt physics. *Frontiers in Astronomy and Space Sciences*, *10*, 1096595. https://doi.org/10.3389/fspas.2023.1096595

Ripoll, J.-F., Reeves, G. D., Cunningham, G. S., Loridan, V., Denton, M., Santolik, O., et al. (2016). Reproducing the observed energy dependent structure of Earth's electron radiation belts during storm recovery with an event-specific diffusion model. *Geophysical Research Letters*, *43*(11), 5616–5625. https://doi.org/10.1002/2016GL068869

Ripoll, J.-F., Santolík, O., Reeves, G. D., Kurth, W. S., Denton, M. H., Loridan, V., et al. (2017). Effects of whistler mode hiss waves in March 2013. *Journal of Geophysical Research: Space Physics*, *122*(7), 7433–7462. https://doi.org/10.1002/2017JA024139

Ripoll, J.-F., Thaller, S. A., Hartley, D. P., Cunningham, G. S., Pierrard, V., Kurth, W. S., et al. (2022). Statistics and empirical models of the plasmasphere boundaries from the Van Allen Probes. *Geophysical Research Letters*, *49*(21), e2022GL101402. https://doi.org/10.1029/2022GL101402

Sandel, B. R., Goldstein, J., Gallagher, D. L., & Spasojevic, M. (2003). Extreme ultraviolet imager observations of the structure and dynamics of the plasmasphere. *Space Science Reviews*, *109*, 25–46. https://doi.org/10.1007/978-94-010-0027-7_2

Sheeley, B., Moldwin, M., Rassoul, H., & Anderson, R. (2001). An empirical plasmasphere and trough density model: CRRES observations. *Journal of Geophysical Research*, *106*(A11), 25631–25641. https://doi.org/10.1029/2000JA000286

Spasojevic, M., Goldstein, J., Carpenter, D. L., Inan, U. S., Sandel, B. R., Moldwin, M. B., & Reinisch, B. W. (2003). Global response of the plasmasphere to a geomagnetic disturbance. *Journal of Geophysical Research*, *108*(A9), 1340. https://doi.org/10.1029/2003JA009987

Storey, L. R. O. (1953). An investigation of whistling atmospherics. *Math. Phys. Sci.*, *246*, 246113–246141. https://doi.org/10.1098/rsta.1953.0011

Thaller, S. A., Wygant, J. R., Cattell, C. A., Breneman, A. W., Tyler, E., Tian, S., et al. (2019). Solar rotation period driven modulations of plasmaspheric density and convective electric field in the inner magnetosphere. *Journal of Geophysical Research: Space Physics*, *124*(3), 1726–1737. https://doi.org/10.1029/2018JA026365

Torkar, K., Nakamura, R., Wellenzohn, S., Jeszenszky, H., Torbert, R. B., Lindqvist, P. A., et al. (2019). Improved determination of plasma density based on spacecraft potential of the magnetospheric multiscale mission under active potential control. *IEEE Transactions on Plasma Science*, *47*(8), 3636–3647. https://doi.org/10.1109/tps.2019.2911425

Trotignon, J. G., Décréau, P. M. E., Rauch, J. L., Randriamboarison, O., Krasnoselskikh, V., Canu, P., et al. (2001). How to determine the thermal electron density and the magnetic field strength from the Cluster/Whisper observations around the Earth. *Annals of Geophysics*, *19*(10/12), 1711–1720. https://doi.org/10.5194/angeo-19-1711-2001

Tu, J., Horwitz, J., Song, P., Huang, X., Reinisch, B., & Richards, P. (2003). Simulating plasmasphere field-aligned density profiles measured with IMAGE/RPI: Effects of ion heating and refilling. *Journal of Geophysical Research*, *108*(A1), 1017. https://doi.org/10.1029/2002JA009468

Wygant, J. R., Bonnell, J. W., Goetz, K., Ergun, R. E., Mozer, F. S., Bale, S. D., et al. (2013). The electric field and waves instruments on the radiation belt storm probes mission. *Space Science Reviews*, *179*(1-4), 183–220. https://doi.org/10.1007/s11214-013-0013-7